

Inner Magnetosphere: Reporter's Review

“Structure, dynamics and coupling of inner magnetosphere”

IUGG 2011
6 July 2011
1630-1715

Yusuke Ebihara

RISH, Kyoto University, Japan

Research areas

2

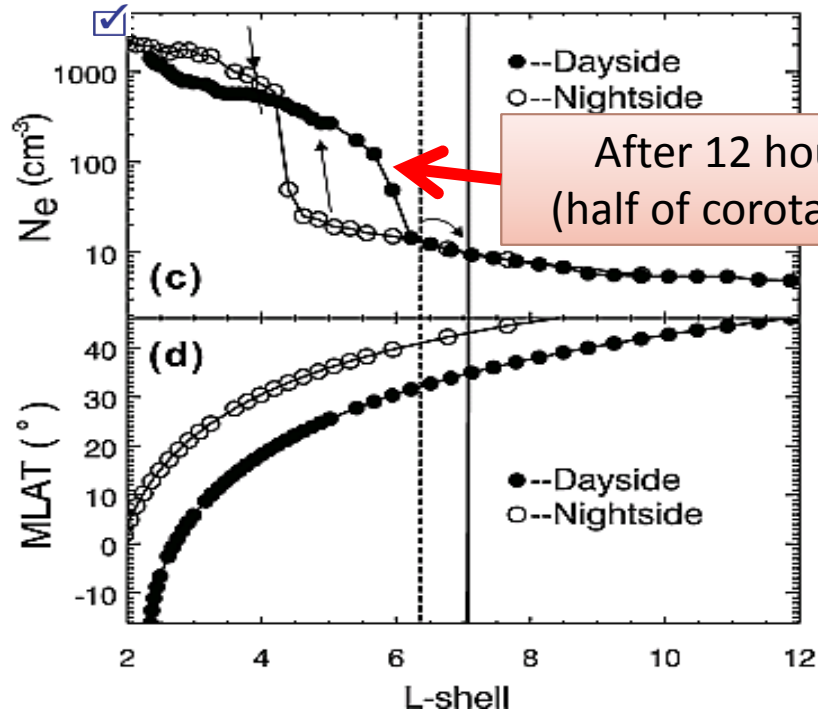
- >350 articles that were published in 2009-2011 have been extensively surveyed.
- The following research areas are covered by this review:
 - Plasmasphere
 - Ring current
 - Radiation belt
 - Particles and fields at $L \leq 6.6$ (geosynchronous orbit)
- The following research areas are covered by other reviewers:
 - ULF waves
 - Wave-particle interaction
 - Aurora
 - Tail ($L > 6.6$)
 - Global dynamics
- All the articles are not covered due to limited time.

- Plasmasphere
- Ring current
- Radiation belt
- Magnetic and electric fields
- Challenging issues

- **Plasmasphere**
- Ring current
- Radiation belt
- Magnetic and electric fields
- Challenging issues

Evolution of plasmasphere

5



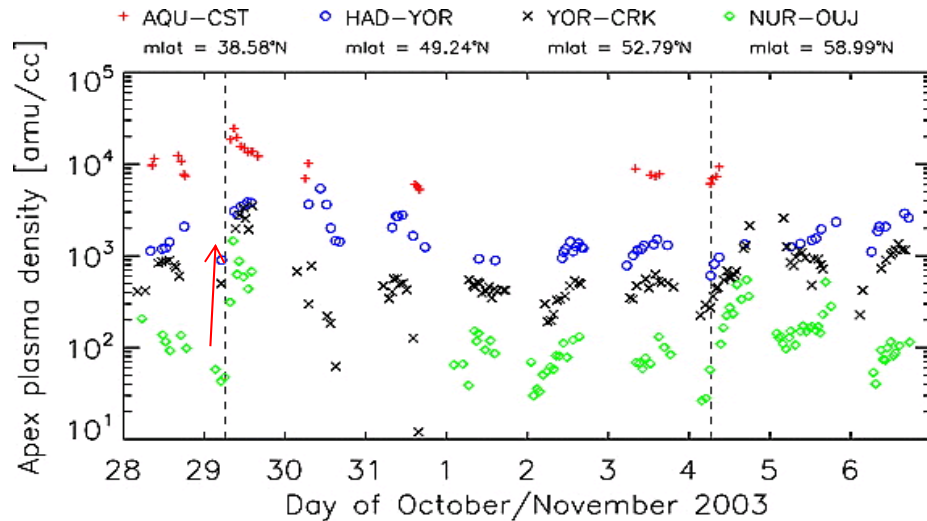
Fu et al. (JGR, 2010)

Electron density profiles obtained by IMAGE/RPI. The plasmapause was located at $L \sim 4.5$ on the nightside. After 12 hours, the plasmapause was located at $L \sim 6$ on the dayside.

- Evolution of plasmasphere is primarily controlled by the fast plasma refilling of the flux tubes from the ionosphere as the flux tubes drift from the nightside to the dayside (Fu et al., JGR, 2010)
- Rotation speed of the plasmapause is weakly correlated with Dst, Kp, AE, the midnight boundary index (MBI), and Joule heating at $L = 2.5$ (Galvan et al., JGR, 2010).
 - Subcorotation of the plasmasphere is due to enhanced auroral zone Joule heating driving equatorward thermospheric winds

Rapid increase in mass density

6

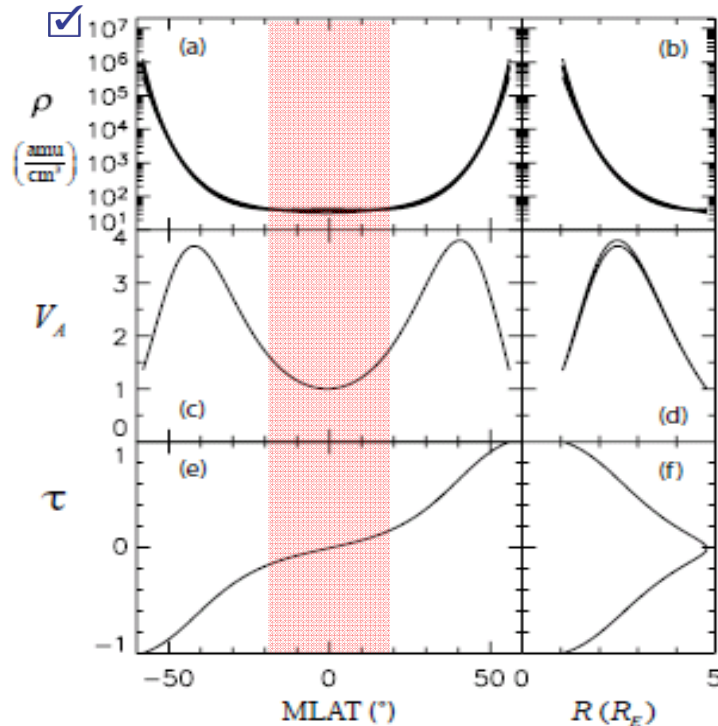


Kale et al. (JGR, 2009)

- During severe storms, a rapid increase in mass density is observed immediately following storm sudden commencement at $2.79 \leq L \leq 3.84$ (Kale et al., JGR, 2009)
 - Rate of density increase was as high as 965 amu/cc/hour, which is much larger than during moderate storms 13-250 amu/cc/hour (Obana et al., 2010).
 - Acceleration due to ponderomotive force? Heating due to precipitating ring current ions and enhanced convection?
 - Rapid ionospheric O⁺ outflow, which is consistent with previous study by Takasaki et al. (2006).

Field-aligned distribution of mass density

7



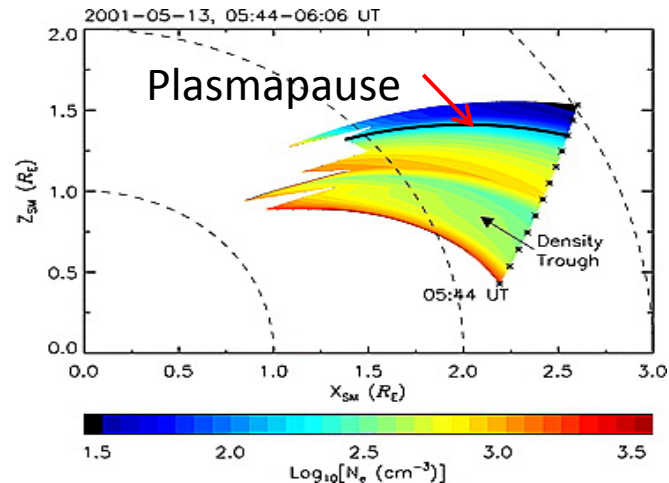
Denton et al. (Ann Geophys, 2009)

- The field line distribution was very flat at $|\text{MLAT}| < 20^\circ$, but very steeply increasing with $|\text{MLAT}|$ for $|\text{MLAT}| > 40^\circ$

Cluster observation of the mass density at L=4.8.

Density trough structure

8



Fu et al. (JGR, 2010)

- “Density trough” is a structure with significantly lower density inside compared to that in the surrounding region (e.g., Horwitz et al., 1990)
- Using data from IMAGE/RPI and DMSP, Fu et al. (JGR, 2010) found that the density trough is a low-density plasmaspheric structure extending from the plasmasphere to the topside ionosphere along the geomagnetic field lines.

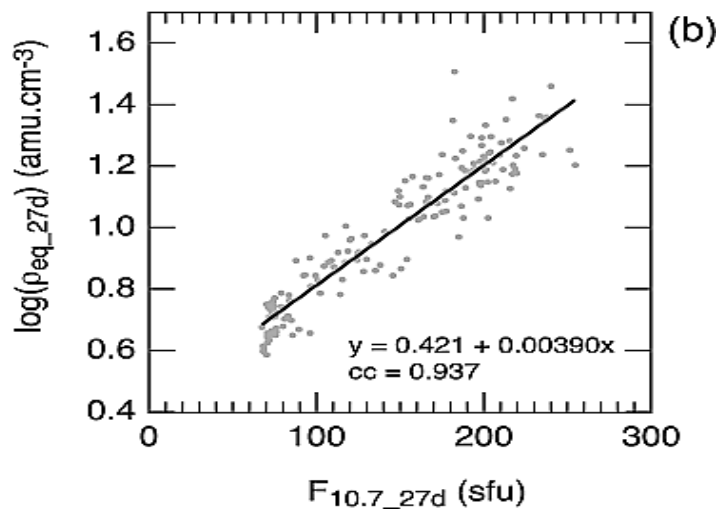
2-D electron density images from $L \sim 2.32$ to $L \sim 4.06$ in the sector of $\text{MLT} = \sim 2130$. The density image is constructed using data from IMAGE/RPI.

The stars on the orbit segment indicate the locations from which the field-aligned density profiles were measured. The thick black line expresses the location of plasmapause.

A density trough is seen in the region from $L \sim 2.32$ to $L \sim 3.00$.

Solar cycle variation of mass density at GEO

9



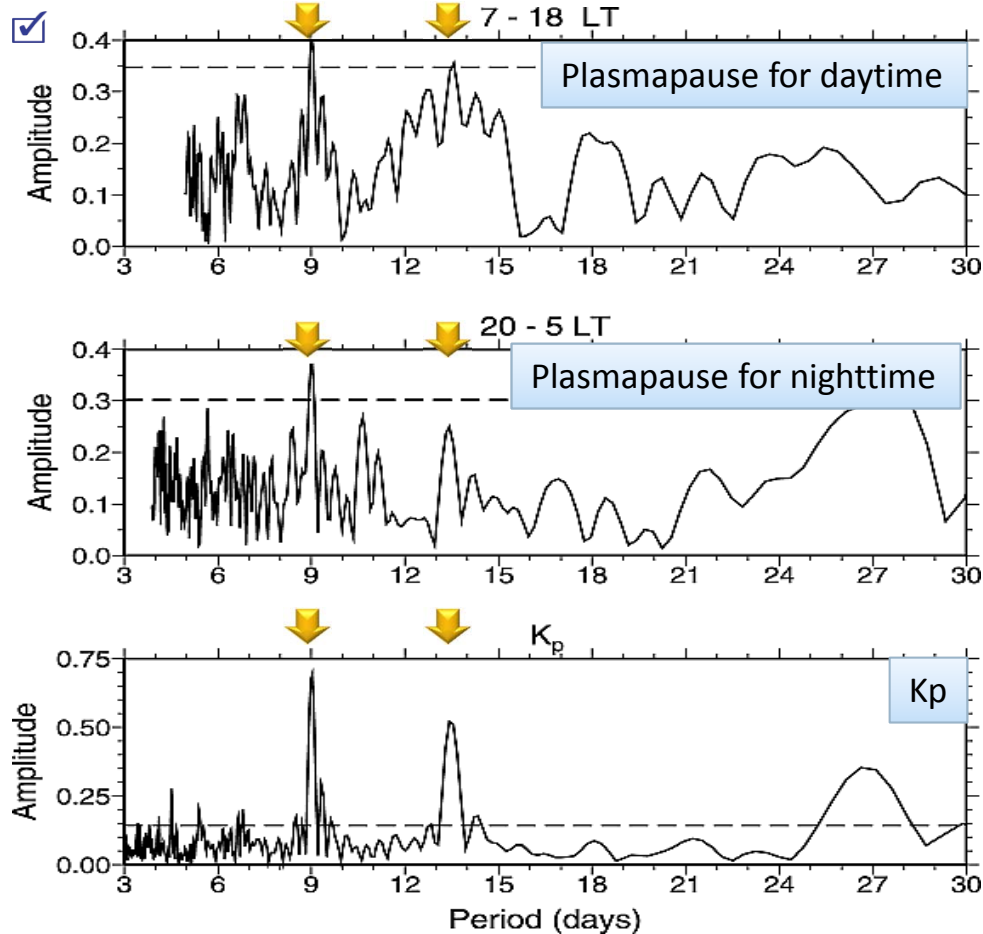
27 day medians of mass density at GEO at $0600 \leq \text{MLT} < 1200$ versus 27 day medians of $F_{10.7}$

Takahashi et al. (JGR, 2010)

- ✓ 27 day medians of mass density is correlated with 27 day medians of $F_{10.7}$ (Takahashi et al., JGR, 2010)
 - $\log \rho_{eq}$ (amu cm⁻³) = $0.42 + 0.0039F_{10.7}$
- Yearly medians mass density is correlated with yearly averaged average of $F_{10.7}$ (Denton et al., JGR, 2011)
 - $\log_{10}(\rho_m) = 0.5089 + 0.003607F_{10.7}$
 - Averaged mass is typically ~ 3.8 at solar maximum and near unity at solar minimum.

9 and 13.5 days oscillation of plasmopause

10



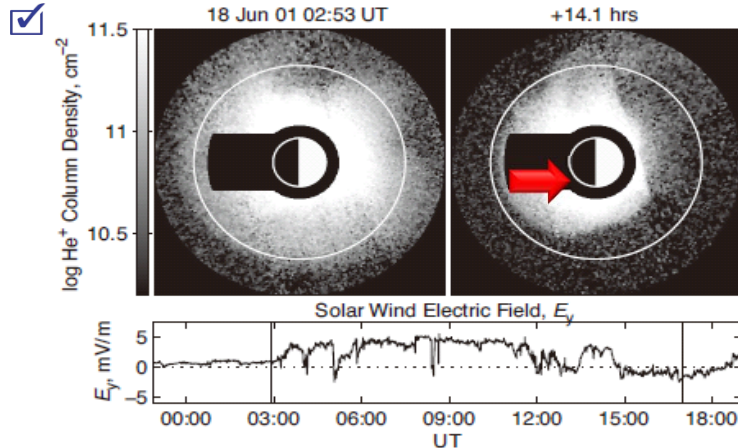
Pedatella and Larson (JGR, 2010)

- The plasmopause oscillates at periods of 9 and 13.5 days during 2008 in connection with recurrent geomagnetic activity due to high-speed solar wind streams.

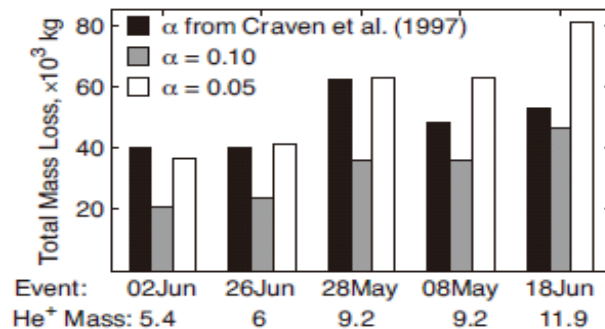
“Period spectrogram” of the plasmopause location determined by GPS TEC measurements for the (top) daytime and (middle) nighttime as well as (bottom) K_p .

Total mass lost

11



Column density of He⁺ before and after the enhancement of eastward solar wind electric field. The plasmasphere is highly eroded.



Total mass of plasma in metric tons removed from the inner magnetosphere for 5 disturbance intervals. They are calculated using to constant He⁺/H⁺ ratio, 0.10 and 0.05.

Spasojevic et al. (Ann Geophys, 2010)

- The total mass lost is found to be in the range of 20 to 80 metric tons
- For each individual case the estimate can vary by over 50% depending on assumed density ratio.

GPS Total Electron Content

12

■ GPS TEC tomography

■ WinTEC algorithm

■ Anghel et al., (JASTP, 2009)

■ Plasmaspheric total electron content (PTEC)

■ Bishop et al. (RS, 2009)

■ Kalman filter technique

■ Carrano et al. (RS, 2009)

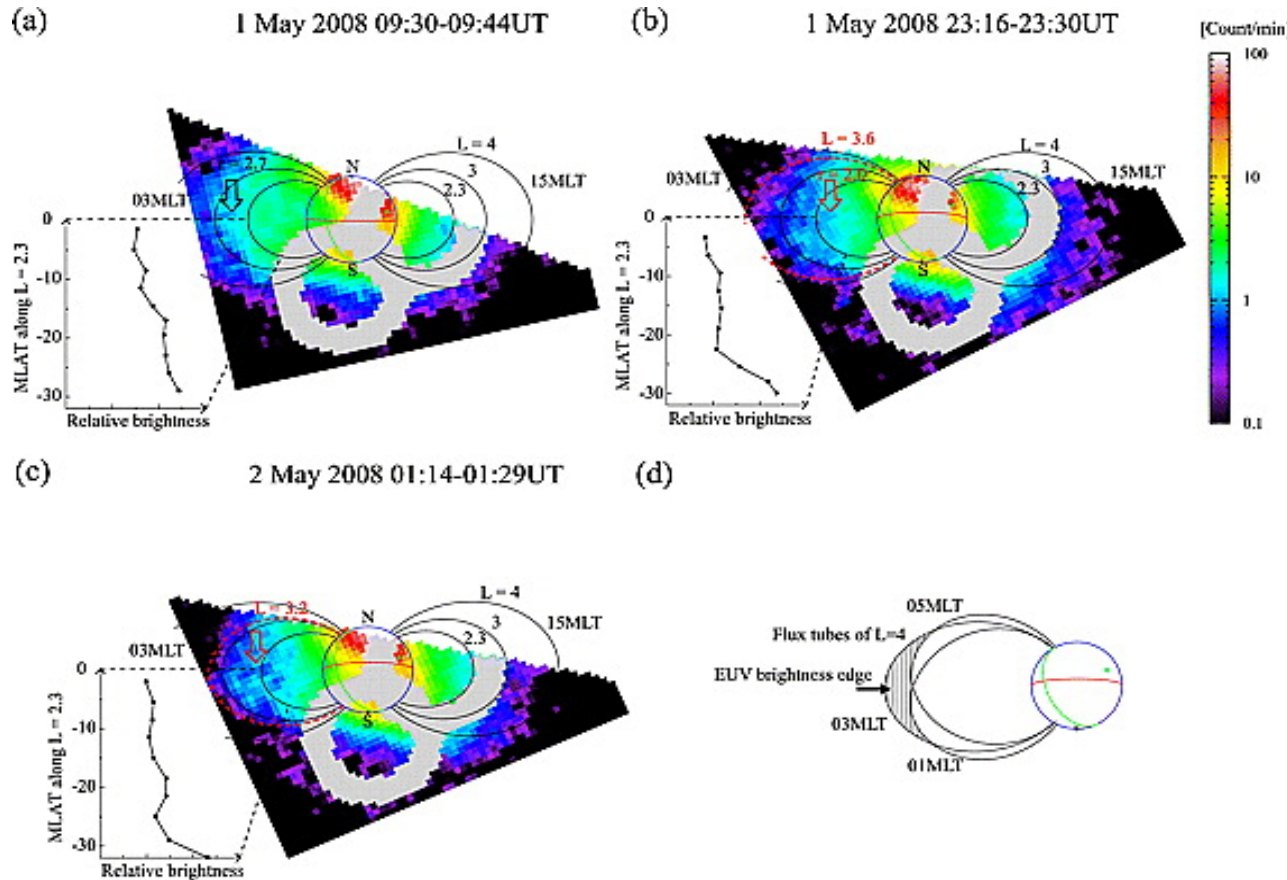
■ Global Assimilation of Ionospheric Measurements

■ Thompson et al. (RS, 2009)

- ☑ By using GPS TEC measurements, several techniques have been developed to globally monitor the structure of the ionosphere and plasmasphere.

Imaging of plasmasphere from Moon

13



- Japanese lunar orbiter “Kaguya” captured He^+ emission from the plasmasphere.
- Outer edge of the He^+ emission moves earthward at a rate of 0.2 R_E /hour.

Yoshikawa et al. (JGR, 2010),
 Murakami et al. (EPS, 2010)
 Obana et al. (JGR, 2010)

“Neutral plasmasphere wind”

14

Gardner and Schunk (RS, 2009)

Enhanced convection electric field (CPCP > 150 kV)



Frictional heating and acceleration of neutrals

Supersonic neutral wind in high-latitude thermosphere ($M \sim 1.5$)

~3 hours delay



Elevated plasma temperature on closed field lines

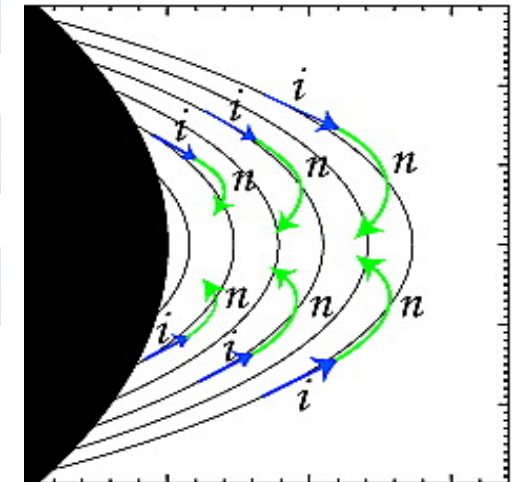


Enhanced ion-neutral charge exchange

Production of neutral streams (Neutral Plasmasphere Wind)



Rain down on the global thermosphere (Neutral Rain)



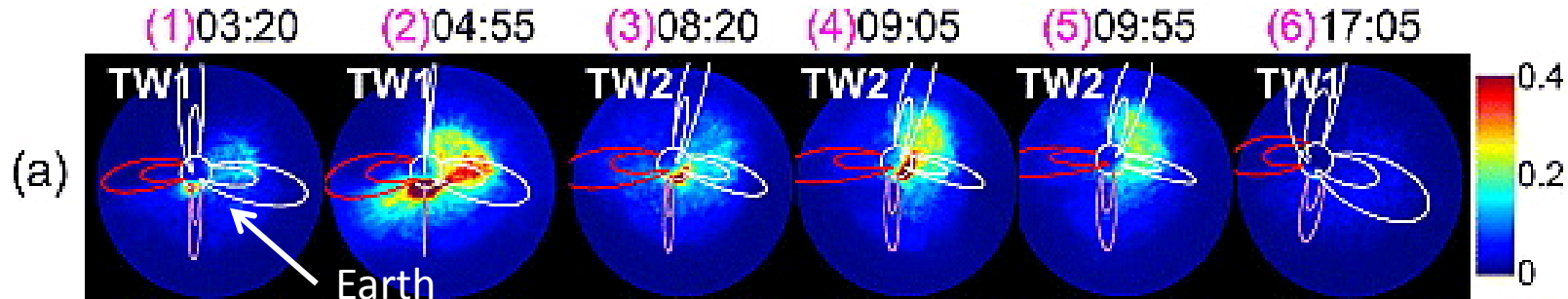
Structure

15

- Plasmasphere
- **Ring current**
- Radiation belt
- Magnetic and electric fields
- Challenging issues

Energetic neutral atom (ENA)

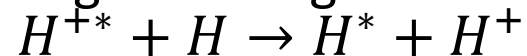
16



TWINS 1 and 2 measurements of ENA (Fok et al., JGR, 2010)



- Energetic neutral atom (ENA) is created when an energetic ion undergoes charge exchange collision with thermal neutral atoms.



- ENA is a powerful tool for investigating global distribution of energetic ions.

Energetic neutral atom (ENA)

17

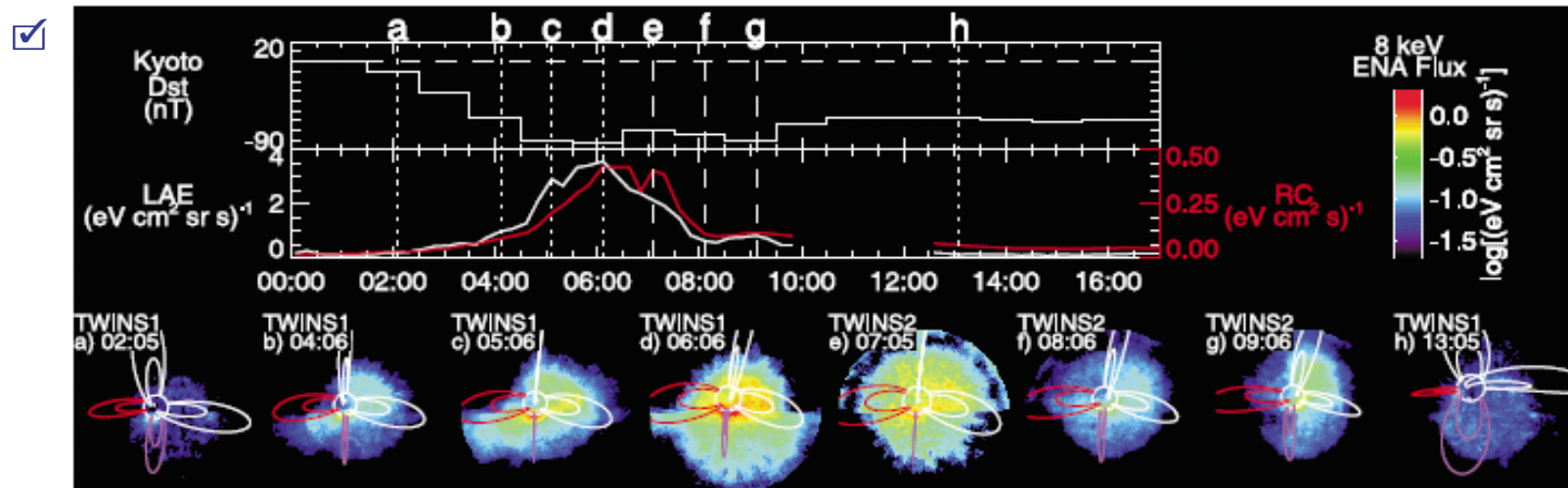
Satellite(s)	Finding(s)	Reference
TWINS 1 and 2	Simulation with time-varying B-field agrees observation.	Fok et al. (JGR, 2010)
	Evolution of global extent and energetics of injected plasma.	Grimes et al. (JGR, 2010)
	Low altitude emissions are the brightest first during the main phase, followed by high altitude emissions during the recovery.	Valek et al. (JGR, 2010)
TC 2	High energy flux of injected plasma on the duskside/nightside.	Lu et al. (JGR, 2010)
IMAGE and TC 2	An initially strongly asymmetric ring current becomes more symmetric.	McKenna-Lawlor et al. (JGR, 2010)
STEREO B	Maximum flux at midnight for 5-20 keV and at 2240 MLT for 20-90 keV.	Wang et al. (GRL, 2010)

Two different populations of ENA

18

Valek et al. (JGR, 2010)

- Low-altitude emissions ($<2 R_E$) of ENA are the result of precipitating ions which undergo multiple charge exchange and stripping collisions with the oxygen exosphere.
- High-altitude emissions ($>2 R_E$) of ENA come from trapped ions in the inner magnetosphere.
- Low-altitude emissions (precipitating H^+) were enhanced first during the storm main phase, followed by the high-altitude emissions (trapped H^+) during the recovery phase.



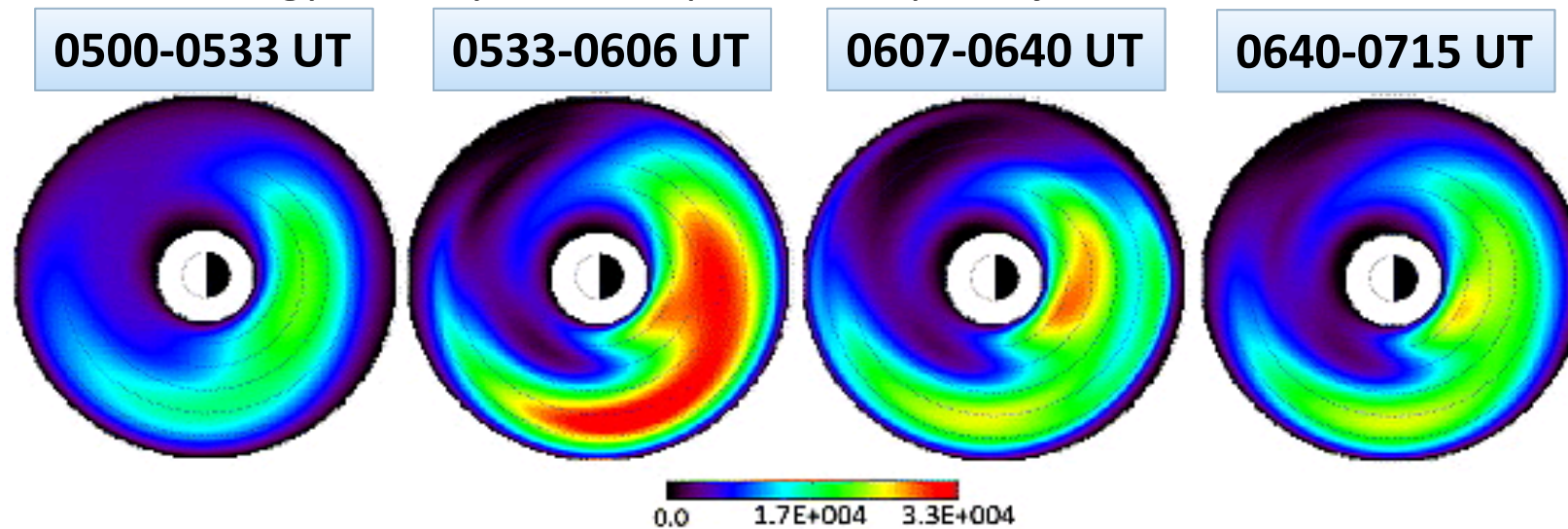
The evolution of the ENA emissions. (top) Dst and the low-altitude emission (LAE) and ring current (RC) indices. LAE index (white curve) is the peak flux per pixel measured within $2R_E$. RC index (red curve) is the integral of flux over the TWINS FOV, not including the region inside of $2R_E$.

Evolution of injected H^+ after a substorm

19

Grimes et al. (JGR, 2010)

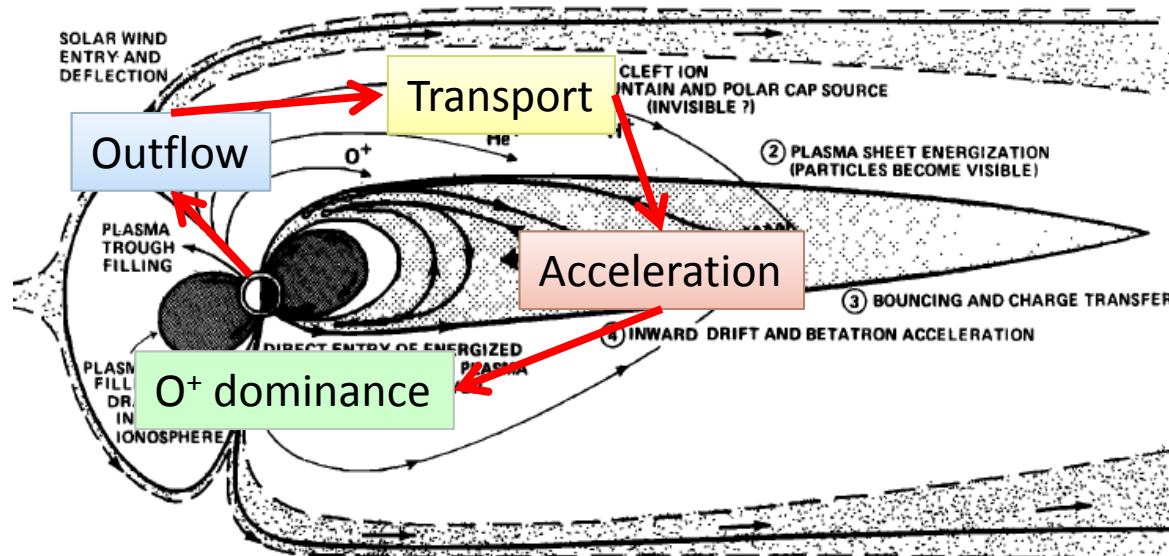
- The energy density in the ring current is enhanced by almost a factor of 2 and stretches from postmidnight to dusk immediately following injections.
- The energy density then drops back to pre-injection levels within 1-2 h.



5–30 keV equatorial energy density profiles for 0500–0715UT on 10 August 2008. The energy density was obtained by using data from TWINS 1 and 2.

O⁺ issues

20



Chappell et al. (JGR, 1987)



- O⁺ ions sometimes dominate in the inner magnetosphere.
- The prime issues are the mechanisms regarding **outflow**, **transport**, and **acceleration** of O⁺ ions.
- Impact of O⁺ ions on the magnetospheric dynamics is also an issue.

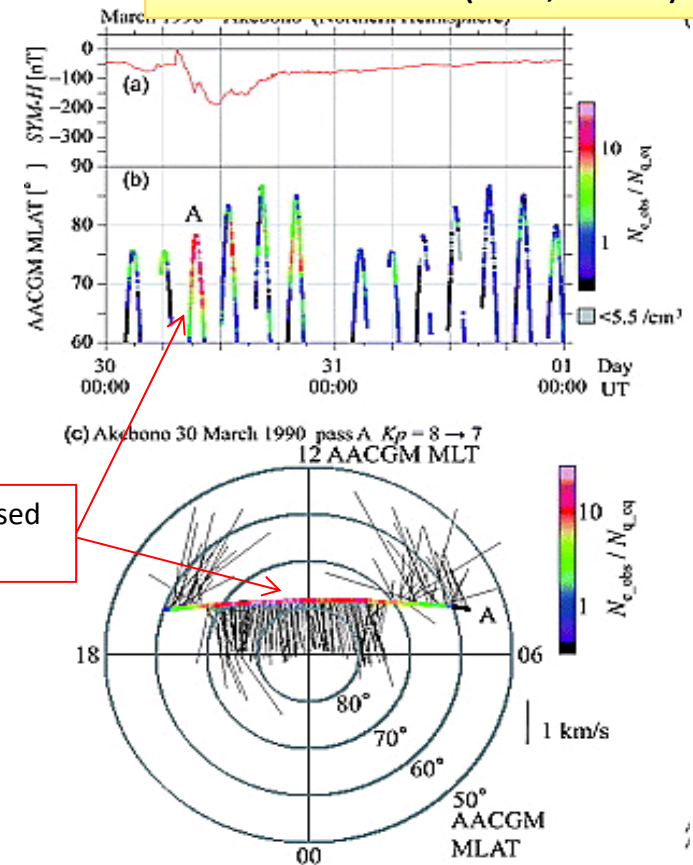
Dense outflowing O⁺ ions

21



- Very dense outflowing O⁺ was found in the poleward of cusp at ~9000 km during storms (Kitamura et al., JGR, 2010).
- Density was increased by a factor >10.
- Upward speeds 4-10 km/s (=1.3-8.4 eV)

Kitamura et al. (JGR, 2010)



Density of O⁺ is increased by a factor >10.

Transport of O⁺ ions

22

- During storms, in lobe, tailward streaming O⁺ increases. When the lobe O⁺ population reaches the plasma sheet, O⁺/H⁺ ratio increases (Kistler et al., JGR, 2010).
- Some of the pre-existing, quiet time, in-transit O⁺ populations are captured on magnetic field lines during these reconfigurations during reconfigurations. This immediately leads to the growth of the storm-time ring current. (Peterson et al., JASTP, 2009).
- Transport path of outflowing O⁺ in the lobe shows dawn/dusk asymmetry according to IMF B_y (Liao et al., JGR, 2010).

Impact of outflowing O^+ on ring current

23

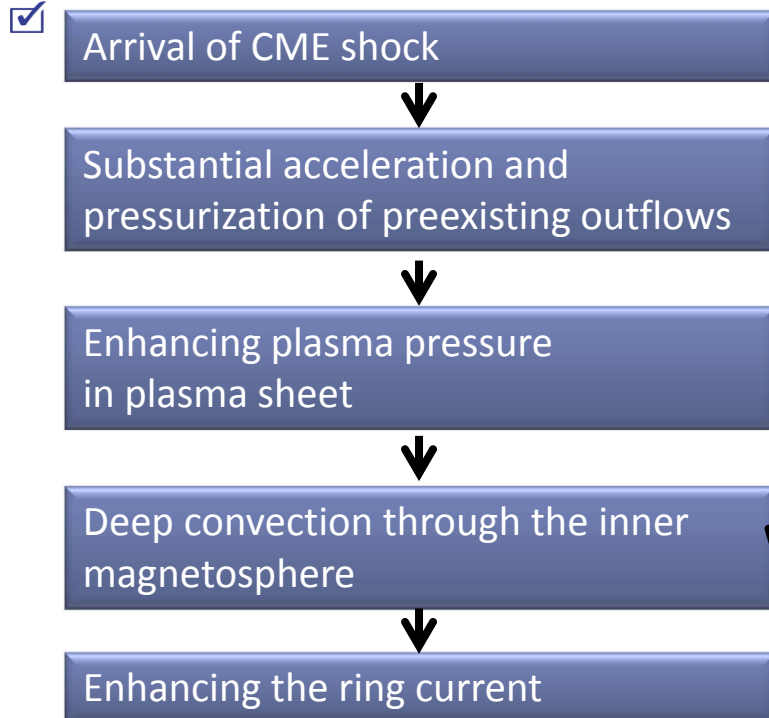
Simulation	Outflow model	Reference(s)
Multifluid LFM	Strangeway et al. (2005) with regulating function	Brambles et al. (JGR, 2010)
Multifluid MHD (Winglee) +single particle	Beam (400 m/s) with isotropic Maxwellian.	Cash et al. (JGR, 2010a,2010b)
LFM + single particle + CRCM	Strangeway et al. (2005) +parallel E-field depending on upward FAC	Fok et al. (JGR, 2011) Moore et al. (JGR, 2010)
Multispecies BATS-R-RUS + 125 flux tubes	Self-contained description of polar wind	Glocer et al. (JGR, 2009)
MHD + single particle	Strangeway et al. (2005)	Perroomian et al. (JGR, 2011)
BATS-R-US+PWOM+RIM+RAM-SCB	Self-contained description of polar wind	Welling et al. (JGR, 2011)

- ✓ Several global simulations have been performed to investigate possible impact of outflowing O^+ on the ring current.
 - Strangeway et al. (2005) provide an empirical model of outflowing O^+ as a function of DC Poynting flux and precipitating electrons.

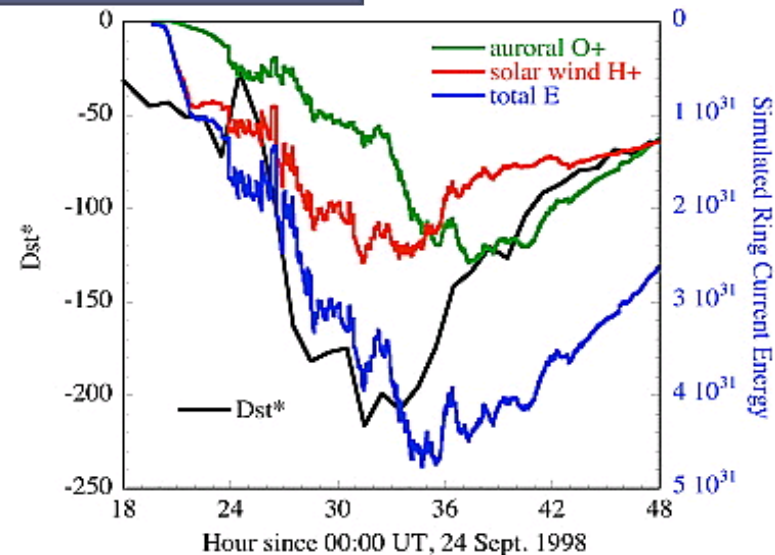
Impact of outflowing O^+ on ring current

24

Moore et al. (JGR, 2010)



Southward turning of IMF

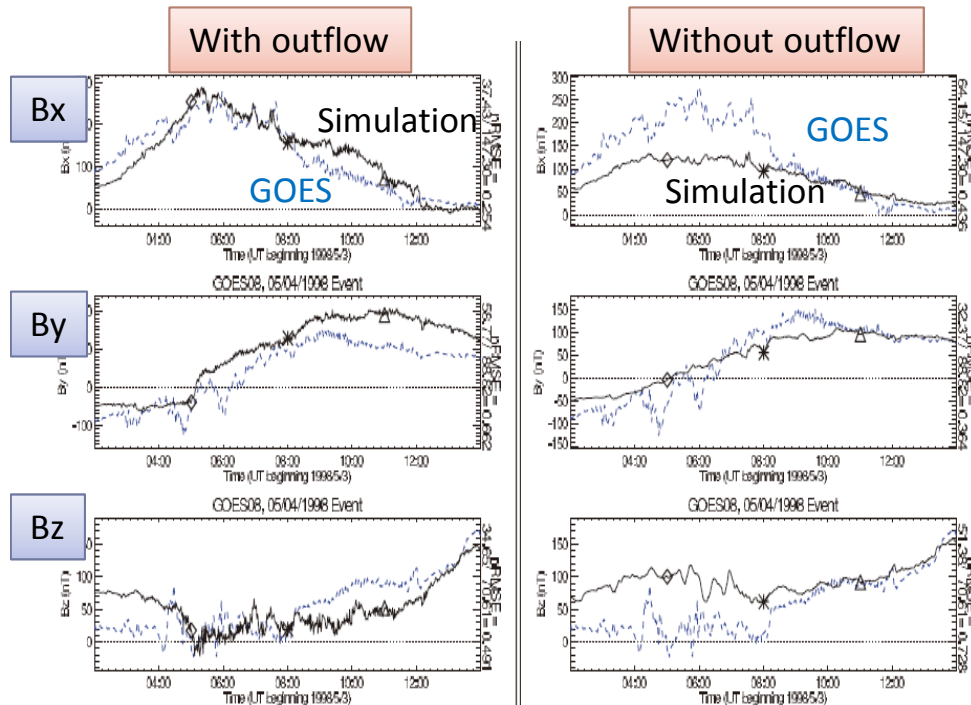


Early in the storm, Dst was dominated by solar wind H^+ , but after several hours, O^+ became comparable in pressure contribution as protons faded and O^+ increased.

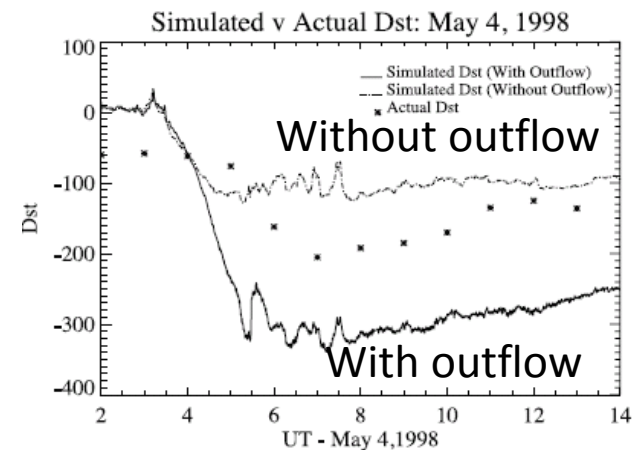
Impact of outflowing O^+ on ring current

25

Glocer et al. (JGR, 2009)



- By including ionospheric outflow into MHD simulation, magnetic field variations get closer to GOES observation.
- Additionally, they find that the outflow causes a strong decrease in Dst and in the cross-polar cap potential (as suggested by Winglee et al. 2002).



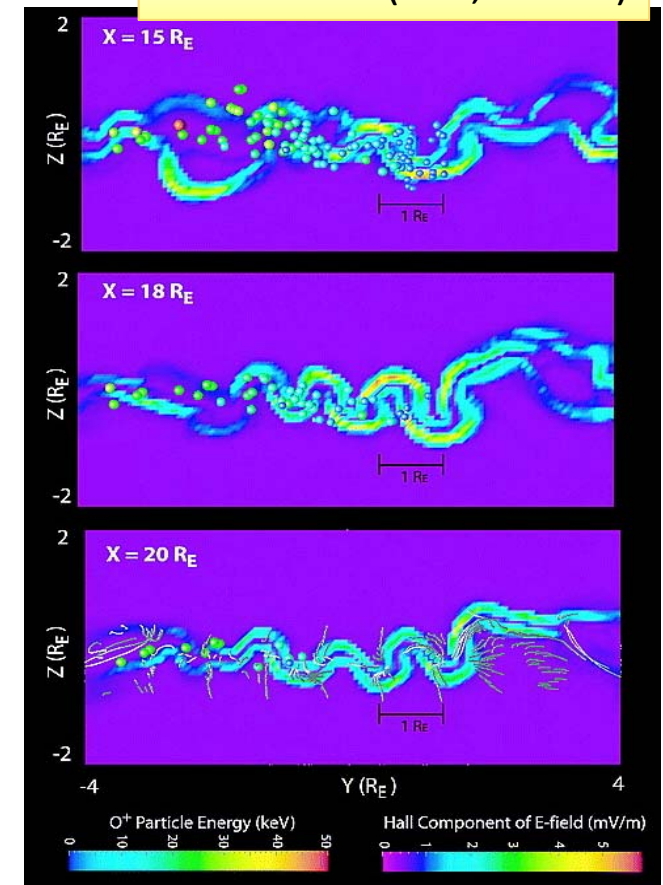
Impact of outflowing O^+ on magnetosphere

26

- Outflowing O^+ gets energized in the small-scale structures in the current sheet.
- High-resolution simulation resolves these small-scale processes within a thin (< 1000 km) current sheet. Simulations with coarse grid resolution underestimate the energization of ring current particles.
- They also found that during the early part of the storm, high-latitude outflow regions between 00 and 06 MLT are the most efficient sectors at contributing particle density to the ring current, whereas during the main phase of the storm, there is more even contribution from all MLTs.

- ☑ Hall component of the electric field as seen from the down tail region (X-Z plane) showing the kinking of the current sheet. Once inside the current sheet, O^+ convects duskward following the sinusoidal kinks.

Cash et al. (JGR, 2010a)

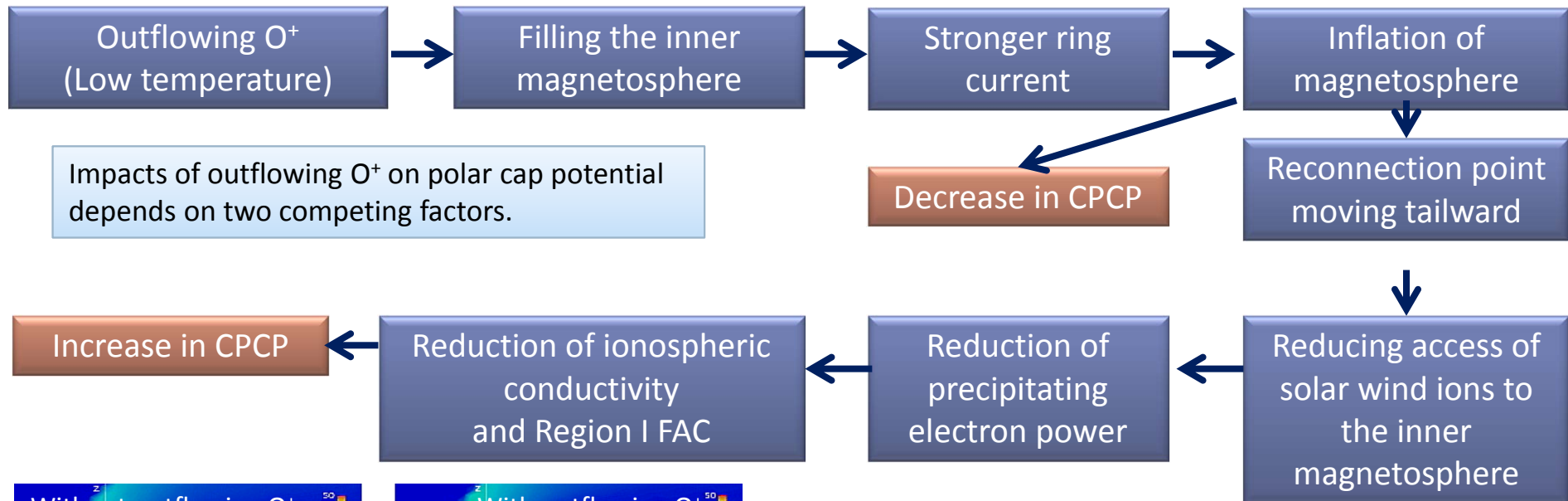


Impact of outflowing O^+ on magnetosphere

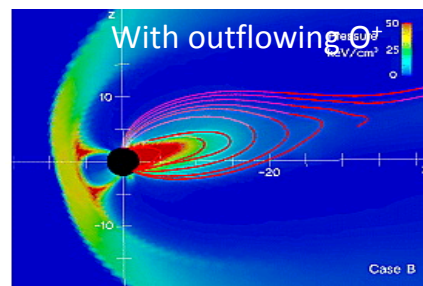
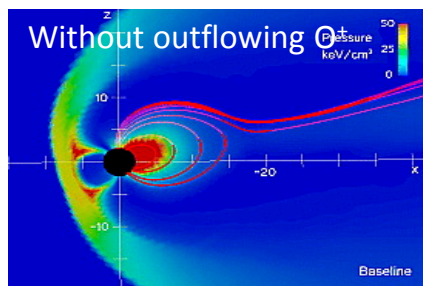
27



Brambles et al. (JGR, 2010)



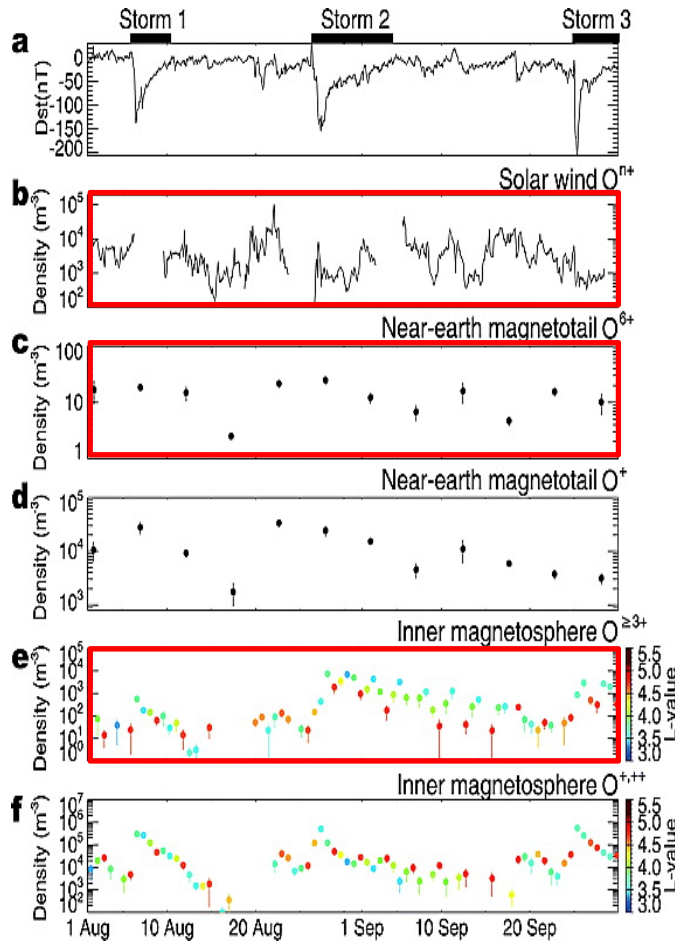
Impacts of outflowing O^+ on polar cap potential depends on two competing factors.



Total plasma pressure for (left) baseline (right) and case B in GSM x-z plane showing select nightside magnetic field lines.

High charge state oxygen ion in ring current

28



Dst



Solar wind O^{n+}
(ACE)

Near-earth plasma sheet O^{6+}
(Geotail)

Inner magnetosphere $O^{\geq 3+}$
(Polar)

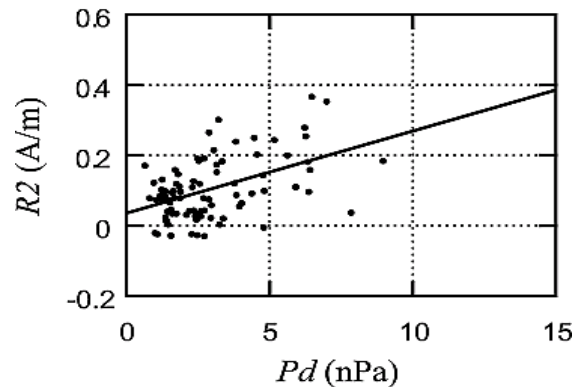
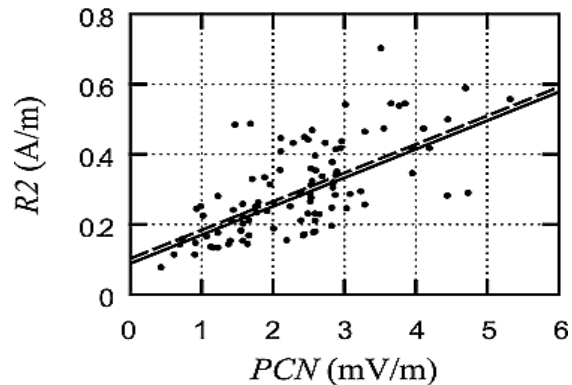
Ebihara et al. (JGR, 2009a)

- High charge state O ions are found to be enhanced during storms in the inner magnetosphere, together with O^+ .
- High charge state O ions are the solar wind origin.
- High charge state O ions were not enhanced in solar wind and near-Earth plasma sheet in association with the storms.
- Suggesting direct entry of solar wind O into the inner magnetosphere?

Driver of Region 2 FAC

29

Nakano et al. (JGR, 2009)



$$-80 \leq D_{st}^* < -50$$

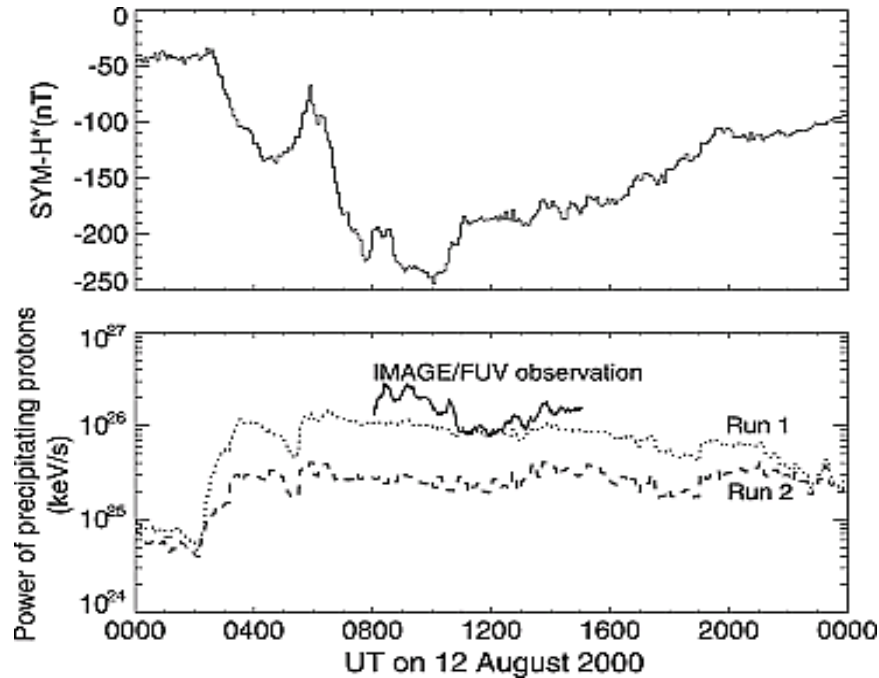


- Region 2 field-aligned current intensity is correlated with
 - the polar cap electric field,
 - and the solar wind dynamic pressure during magnetic storms.
- Region 2 current can be driven by
 - intensification of the ring current,
 - transition of angle between the magnetic pressure gradient and plasma pressure gradient.

Rapid decay of ring current (FLC scattering)

30

Ebihara et al. (JGR, 2011)



Power of precipitating protons
(simulation and IMAGE/FUV auroral observation)



- Burton's (1975) empirical model (which predicts Dst) assumes the decay lifetime of 7.7 hours.
- But, the physical meaning of the lifetime is not understood.
- Storm-time magnetic field is stretched enough to scatter ions, resulting in precipitation into ionosphere.
- This is called the Field Line Curvature (FLC) scattering.
- Ebihara et al. (2011) performed CRCM, and found that the ring current decays with a lifetime of ~6 hours.

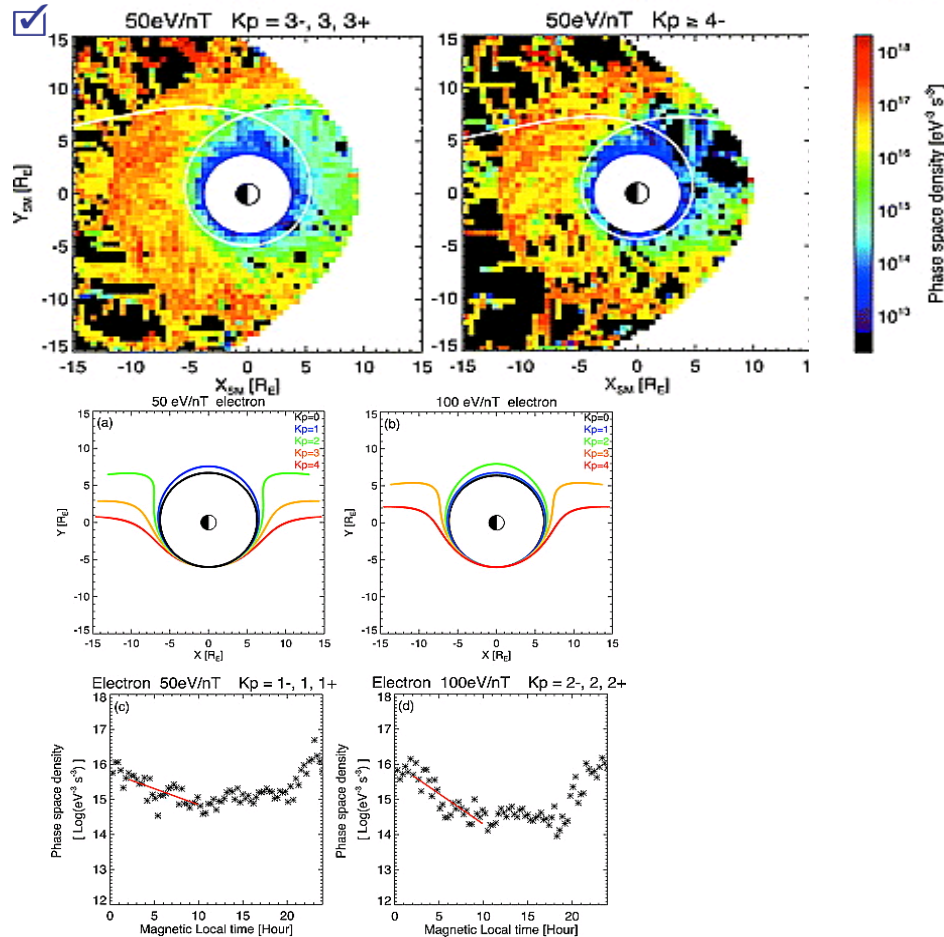
Rapid decay of ring current (EMIC)

31

- EMIC waves can produce efficient pitch angle scattering of energetic (tens of keV) protons, yielding a rapid decrement in the flux with a time scale of a few hours (Xiao et al., JASTP, 2011).
 - EMIC waves are observed in limited region?

Decay of keV electrons

32



Kurita et al. (JGR, 2011)

- Kurita et al. (JGR, 2011) compiled phase space density of electrons acquired by THEMIS, and displayed it on the equatorial plane as a function of Kp.
- Assuming wave parameters, they estimated the decay rates due to the pitch angle scattering by the chorus waves as the combination of the decay rates by the lower band and upper band chorus.
- Required wave amplitudes of chorus waves is consistent with the observed averaged amplitudes of chorus waves (>10 pT) (Meredith et al., 2001).

Recent development of ring current simulations

33

- Fully self-consistent simulation of the ring current coupled to electric and magnetic fields.
 - Amano et al. (JGR, 2010)
- Quasi-static self-consistent simulation of the ring current coupled with an MHD simulation.
 - Zaharia et al. (JGR, 2010)

Structure

34

- Plasmasphere
- Ring current
- **Radiation belt**
- Magnetic and electric fields
- Challenging issues

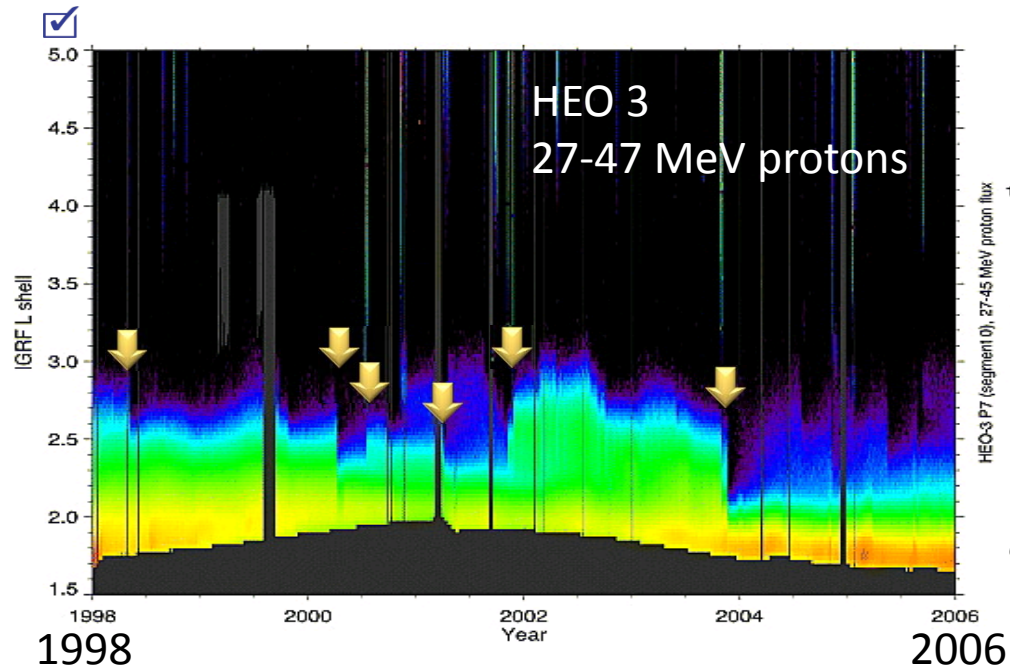
Structure

35

- Plasmasphere
- Ring current
- **Radiation belt (proton belt)**
- Magnetic and electric fields
- Challenging issues

Rapid changes (~ 1 day) in proton belt

36



Color-coded proton flux (27-45 MeV) as a function of L and time from the HEO-3 satellite.

Selesnick et al. (JGR, 2010)

- Trapped proton flux shows clear rapid changes (~ 1 day) at $L < 3$.
- Drift resonance with electric field impulses caused by rapid magnetospheric compression is the likely cause of both solar proton injections and radial shifts of preexisting trapped protons.
- Injection of less than 10 kW of Shear Alfvén Wave from the ground is enough to reduce the trapped energetic protons about 2~3 years.

Structure

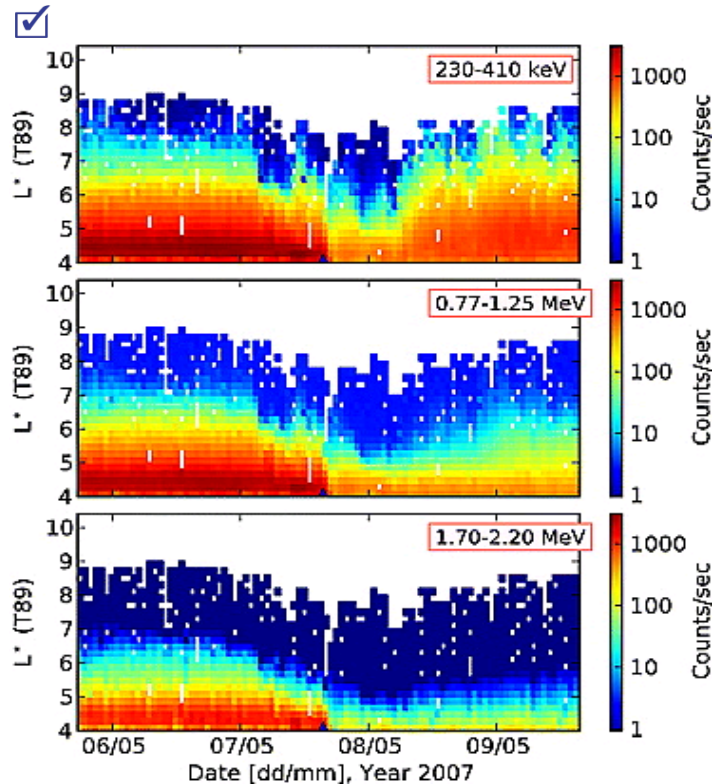
37

- Plasmasphere
- Ring current
- **Radiation belt (electron belt)**
- Magnetic and electric fields
- Challenging issues

Rapid loss of outer belt (~ 2 hours)

38

Morley et al. (GRL, 2010)



GPS constellation

- A rapid loss of energetic (>230 keV) electrons occurred from $4 < L^* < 6$ over all measured energies above 230 keV
- The loss timescale is ~ 2 hours, and the magnetopause is near $L = 8$ which requires unrealistically high outward diffusion rates.
- Current estimates of the loss timescales associated with EMIC waves, plasmaspheric hiss and whistler-mode chorus are too long, even in combination, to explain the observed losses inside $L^*=6$.

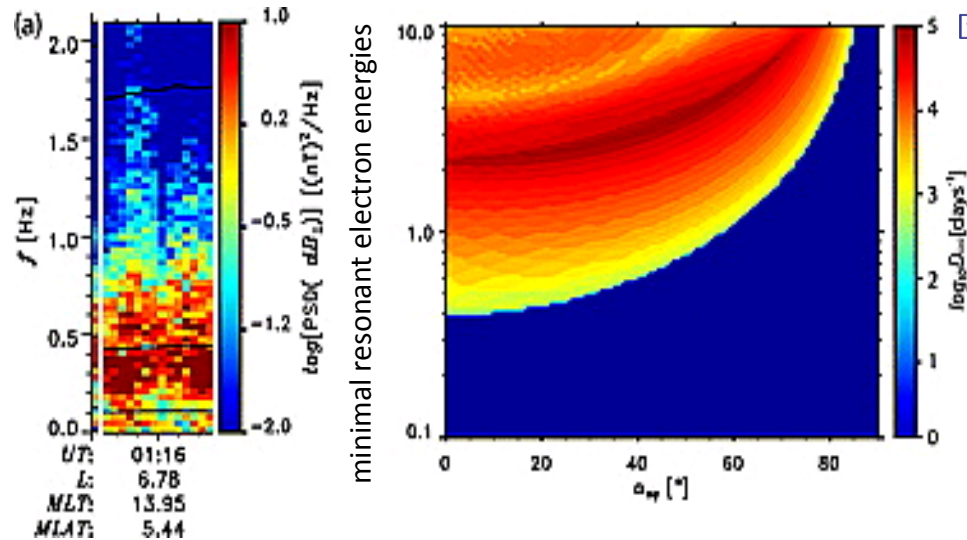
Drift loss to the magnetopause

39

- ☑ ■ Direct loss to the magnetopause is one of the mechanisms for dropout of the outer belt.
 - Ohtani et al. (JGR, 2009)
 - Effective duration of the compression of the dayside magnetosphere is as short as ~30 min.
 - Kim et al. (JGR, 2010)
 - Saito et al. (JGR, 2010)
 - Su et al. (GRL, 2011)
 - Combined magnetopause shadowing and adiabatic transport tend to underestimate energetic electron fluxes in the inner L-shells ($L < 5$), and overestimate them in the outer L-shells ($L > 5$).
 - Combination of magnetopause shadowing, adiabatic transport, radial diffusion, and plasmaspheric hiss gives reasonable result.

Precipitation loss to the ionosphere (EMIC)

40



(left) Dynamic spectrum of waves by AMPTE CCE and (right) bounce-averaged pitch-angle diffusion coefficient as a function of minimum energy of electron cyclotron resonance and equatorial pitch angle.

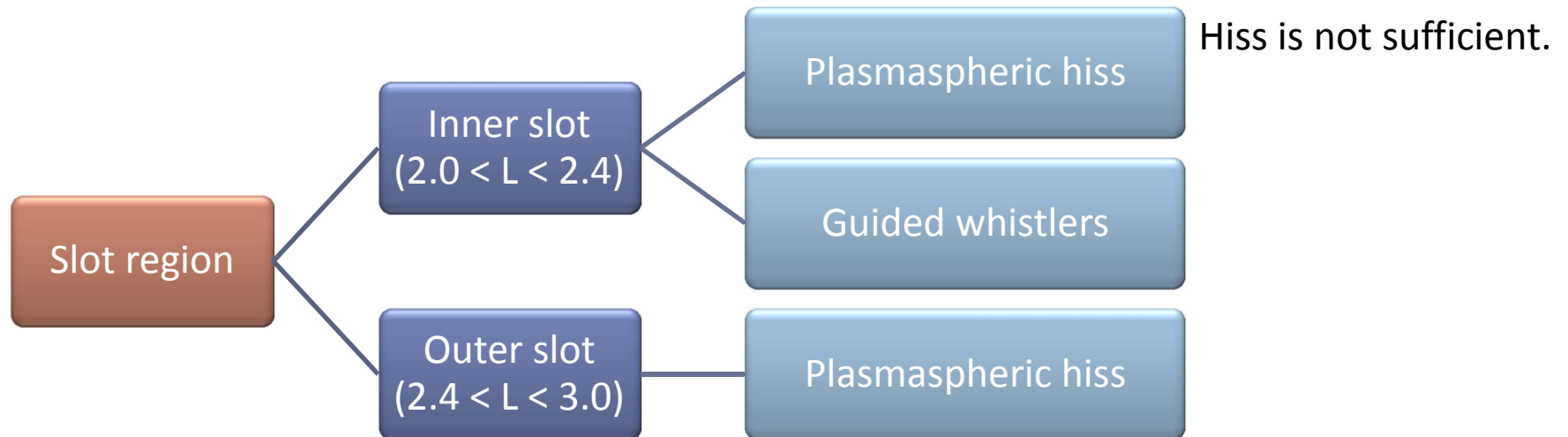
Ukhorskiy et al. (GRL, 2010)

- Large amplitude EMIC waves are observed during the main phase of a storm (Ukhorskiy et al., GRL, 2010).
 - Pitch angle diffusion coefficients are $>10^3 \text{ day}^{-1}$ for $>400 \text{ keV}$ electrons.
 - Minimum lifetime determined by strong diffusion limit is ~ 10 minutes for 1-2 MeV electrons.
- Even moderate EMIC wave amplitudes easily cause resonant electrons to respond nonlinearly. Nonlinear interactions typically lead to advection toward large pitch angles, rather than diffusion toward the loss cone (Albert and Bortnik, GRL, 2009).

Precipitation loss to the ionosphere(slot region)

41

Meredith et al. (JGR, 2009)

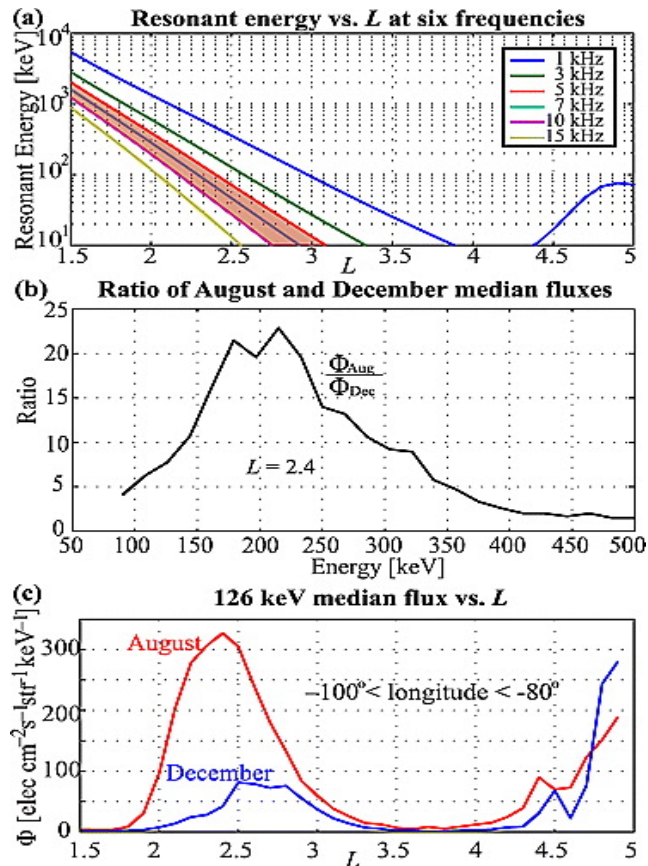


- Decay rate of relativistic electrons measured at low altitudes in the slot region at $L = 2$ is an order of magnitude shorter than theoretical estimates.
- Pitch angle scattering by plasmaspheric hiss ($0.1 < f < 2$ kHz) is the dominant process responsible for electron loss in the outer slot region ($2.4 < L < 3.0$), but hiss alone cannot account for the observed loss timescales at lower L .

Seasonal variation of precipitation loss in slot region

42

Gemelos et al. (GRL, 2009)



- Over the United States, energetic electron fluxes in the slot region (between $L = 2$ and 3) are significantly higher in the northern summer than in the winter.
- Lightning is a significant contributor to the loss of slot region electrons.

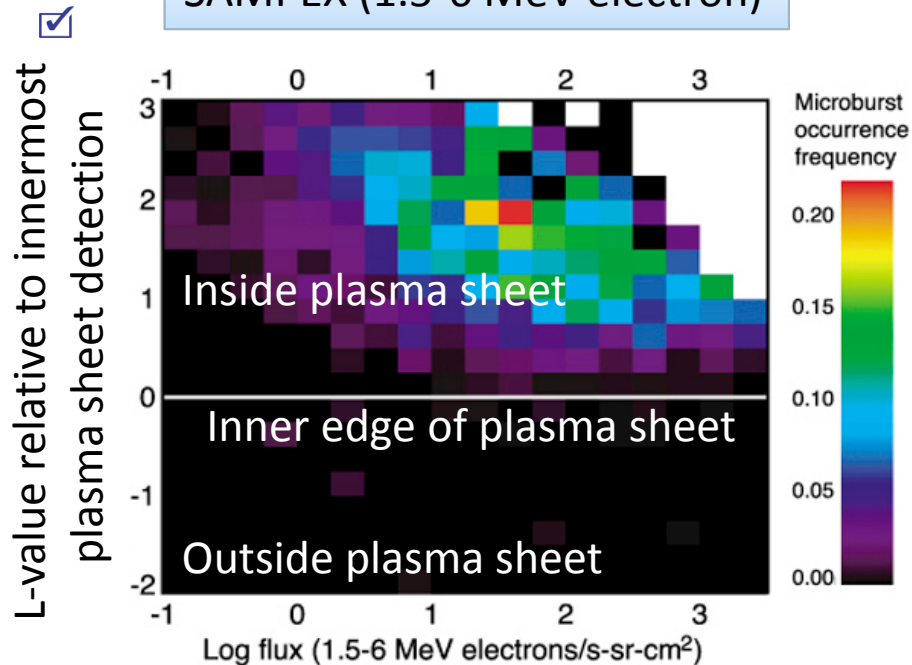
Median 126 keV nighttime flux as a function of L -shell in August and December

Storm-time occurrence of microburst

43

SAMPEX (1.5-6 MeV electron)

Johnston and Anderson (JGR, 2010)

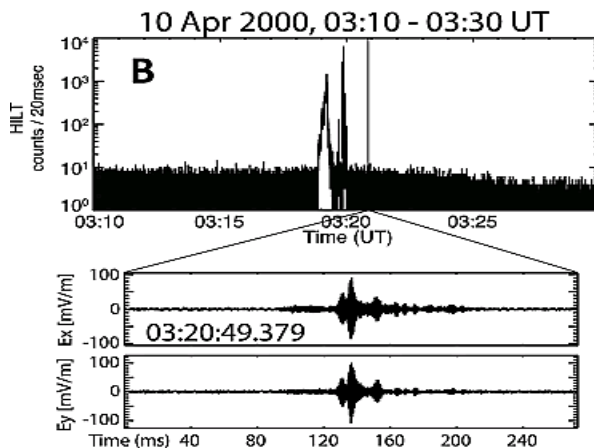
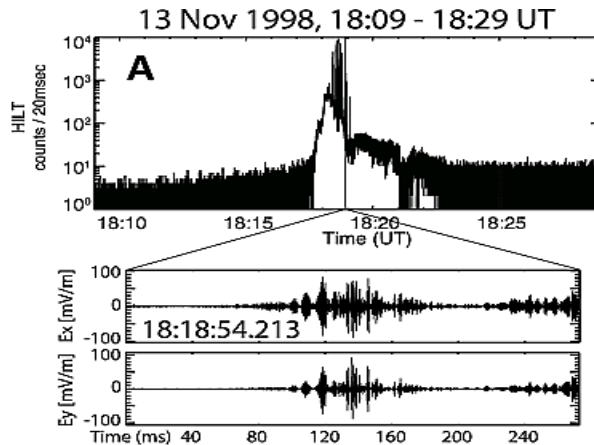


- Microburst is a short-duration phenomenon of electron precipitation.
- Occurrence of relativistic microbursts is associated with a combination of daily averaged 1.5–6 MeV electron fluxes exceeding about 1 particle $s^{-1} sr^{-1} cm^{-2}$ (observed at SAMPEX altitudes) and the presence of soft electrons from the plasma sheet.
- These observations are consistent with the suggestion that microbursts are associated with chorus.

Coincidence of large-amplitude of whistler wave and microburst

44

Kersten et al. (GRL, 2010)

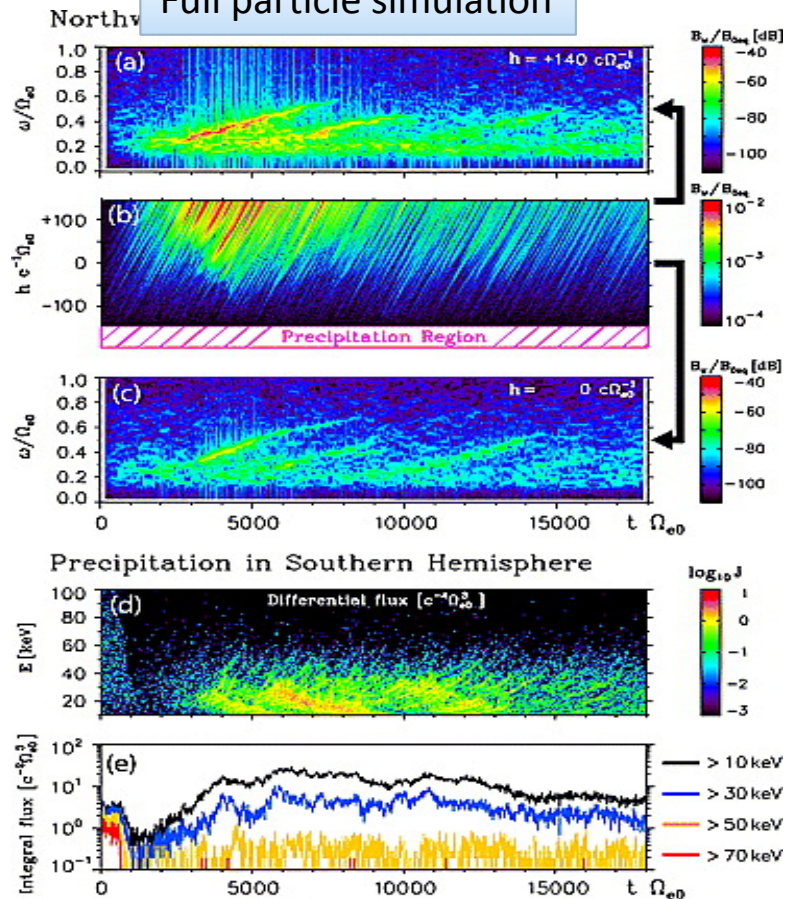


- Wind and STEREO recorded intense whistler-mode waves in the outer nightside equatorial radiation belt with peak-to-peak amplitudes exceeding 300 mV/m.
- During these intervals of intense wave activity, SAMPEX recorded relativistic electron microbursts in near magnetic conjunction with Wind and STEREO.

Simulation of microburst precipitation of electrons

45

Full particle simulation



- Whistler-mode triggered emissions are successfully reproduced by a self-consistent hybrid and full-particle simulations.
- Frequency of a chorus element continuously increases in time.
- The parallel resonant velocity continuously decreases toward lower-velocity ranges resulting in significant scattering of resonant electrons
- Electron microbursts (<1 sec) occur when discrete chorus elements are generated.

Omura et al. (JGR, 2009, 2011),
Hikishima et al. (JGR, 2009, 2010, GRL, 2010)

When, where and why electron precipitation occurs

46



	>300 keV electron	>1 MeV electron
When?	during the main phase	during the recovery phase
Where?	All geographic longitude in both hemispheres	mainly poleward of the South Atlantic Anomaly (SAA) area
Why?	Wave-particle interaction?	Drift loss cone?

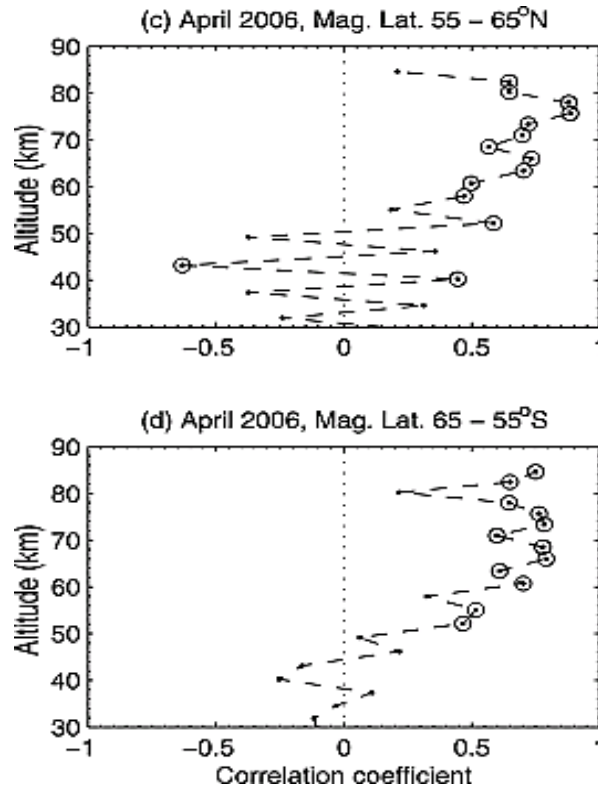
Horne et al. (GRL, 2009)

- Whistler mode chorus waves alone cannot account for the higher MeV precipitation flux during the recovery phase.
- They suggest that whistler mode chorus waves accelerate electrons up to MeV energies during the recovery phase which are then precipitated by EMIC waves.

Impact on mesosphere

47

Verronen et al. (JGR, 2011)

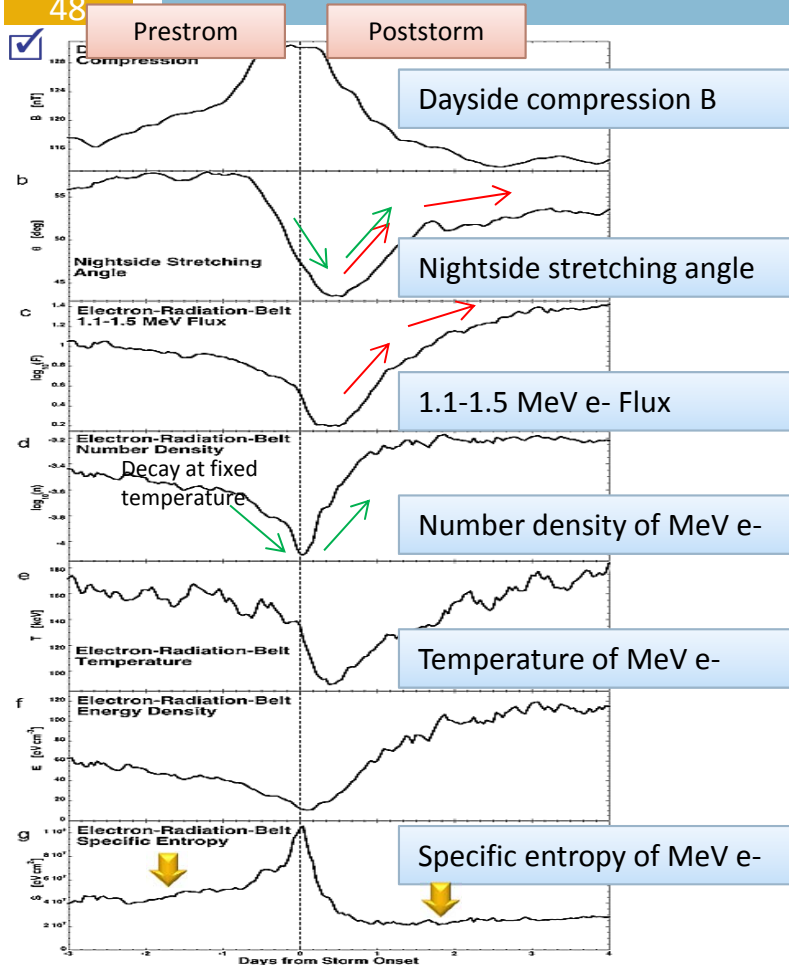


- Verronen et al. (JGR, 2011) found a strong link between 100–300 keV count rate of electrons precipitating into the atmosphere from the radiation belts and mesospheric nighttime OH concentration at 71–78 km altitude.

Correlation coefficients for the daily mean values of 100-300 keV electron count rate and OH concentration.

Decay and recovery of outer belt during CIR-associated storms

48

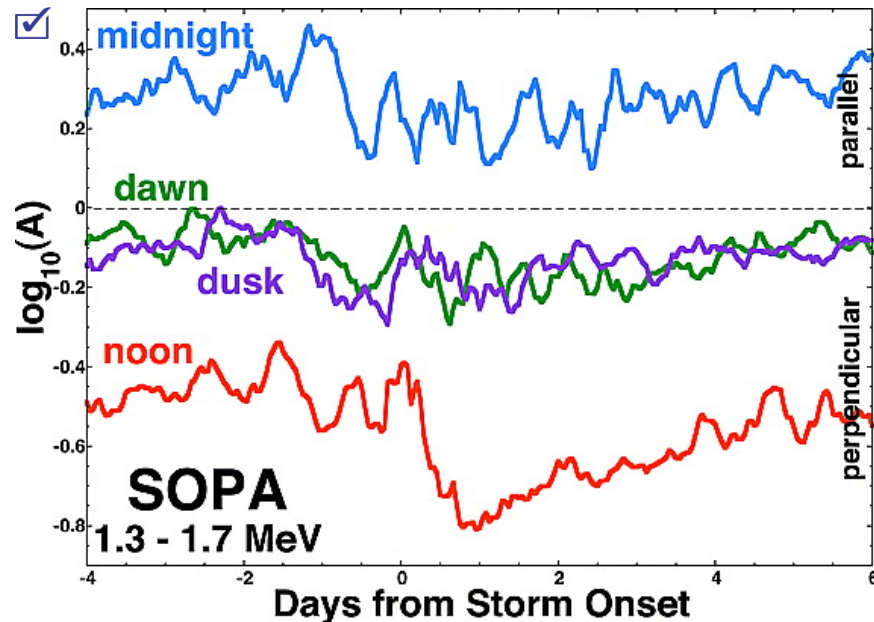


Borovsky and Denton (JGR, 2010a, 2010b),
Denton et al. (JGR, 2010)

- The relativistic electron flux at geosynchronous orbit has a profile that matches the strong-stretching profile (red).
- The number density dropout of the outer electron radiation belt occurs early in the strong-stretching phase and the number density recovery of the outer electron radiation belt commences before the stretching has reached its maximum (green).
- A comparison of geosynchronous field strengths and magnetopause field strengths indicates that magnetopause shadowing plays a role in the radiation belt dropout.
- The specific entropy $S = T/n^{2/3}$ is different after the recovery. This difference implies that the population of radiation belt electrons after recovery is a different population from the population before dropout

Anisotropy of electrons at GEO

49



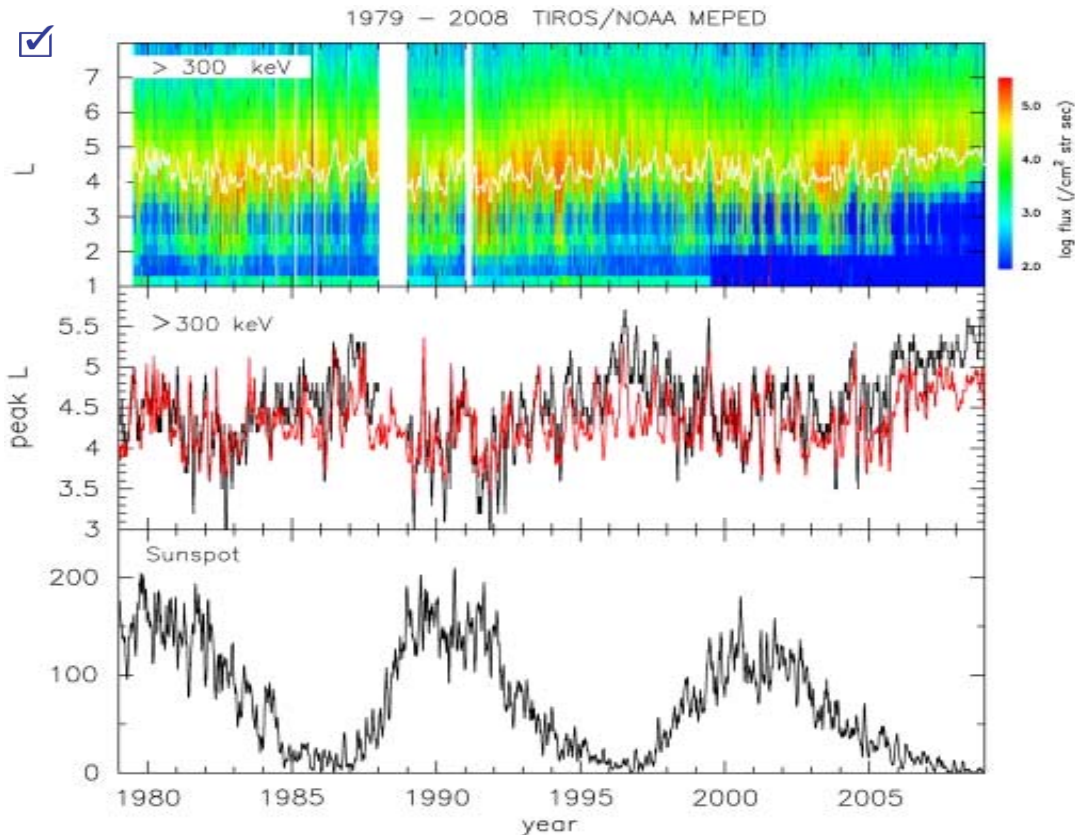
For 42 high-speed-stream-driven storms, the superposed average of the logarithm of the anisotropy parameter A is plotted as a function of time for four local-time bins: midnight (2300–0100 LT), dawn (0500–0700 LT), noon (1100–1300 LT), and dusk

Borovsky and Denton (JGR, 2011)

- The equatorial pitch angle distributions of relativistic electrons at geosynchronous orbit tend to be perpendicular dominated on the dayside and parallel dominated on the nightside.
- Similar tendency was obtained by Gu et al. (JGR, 2011) who investigated flux measurements from CRRES.

Solar cycle dependence of >300 keV electrons

50



30-year interval

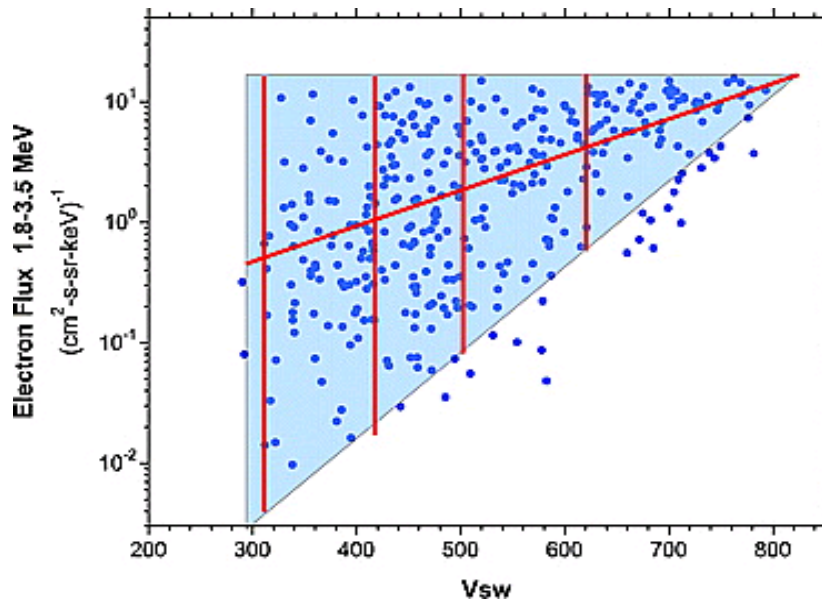
Miyoshi and Kataoka (JASTP, 2011)

- Peak L-value of electron flux with energy >300 is anti-correlated with sunspot number.

Solar wind velocity dependence doubtful?

51

Reeves et al. (JGR, 2011)



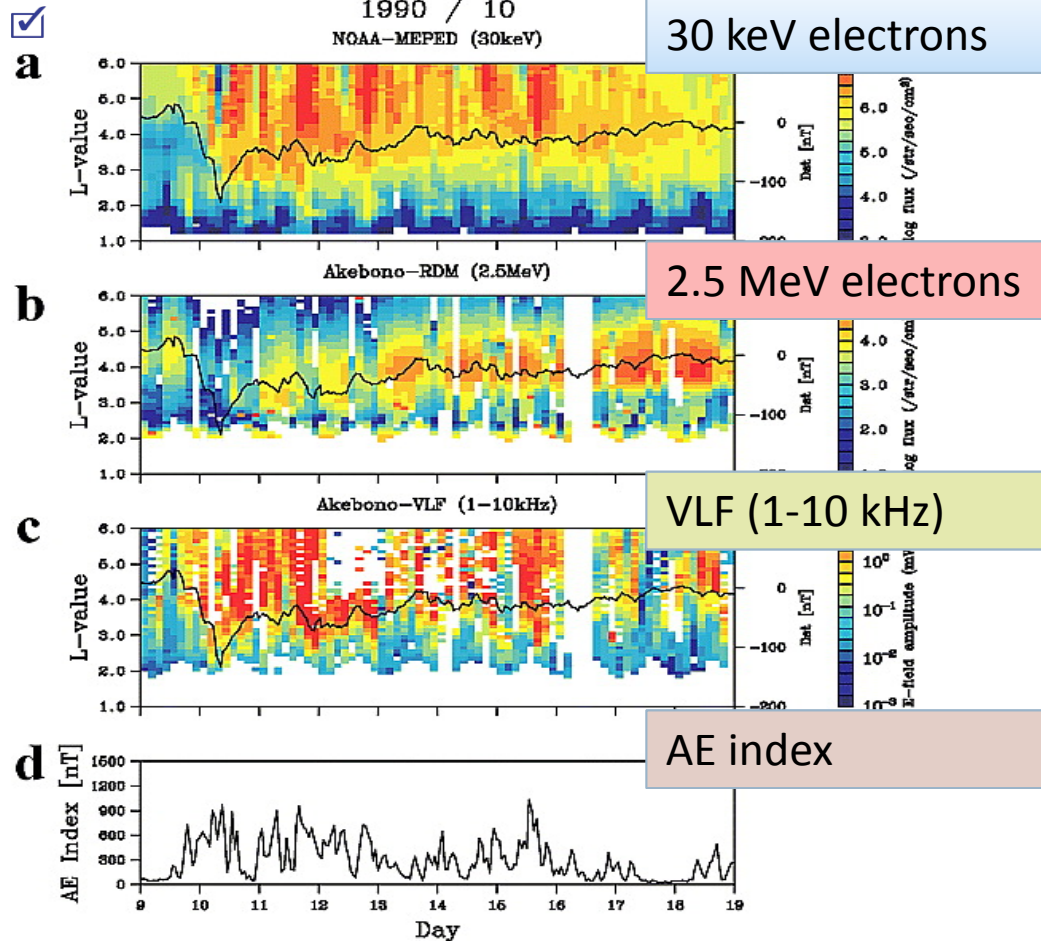
Lower-flux limit depends on V_{sw} , but higher-flux limit does not.



- So far, the solar wind velocity is thought to be a prime driver for intensification of outer radiation belt.
- Electron fluxes (1.8-3.5 MeV) at GEO have a distinct velocity-dependent lower limit but a velocity-independent upper limit.
- The relationship between radiation belt electron fluxes and solar wind velocity is substantially more complex than suggested by previous statistical studies.
- “Conventional wisdom” stating that high-velocity wind drives high-MeV electron fluxes is, in general, either misleading or unsupported.

Hot electrons, chorus, and MeV electrons

52

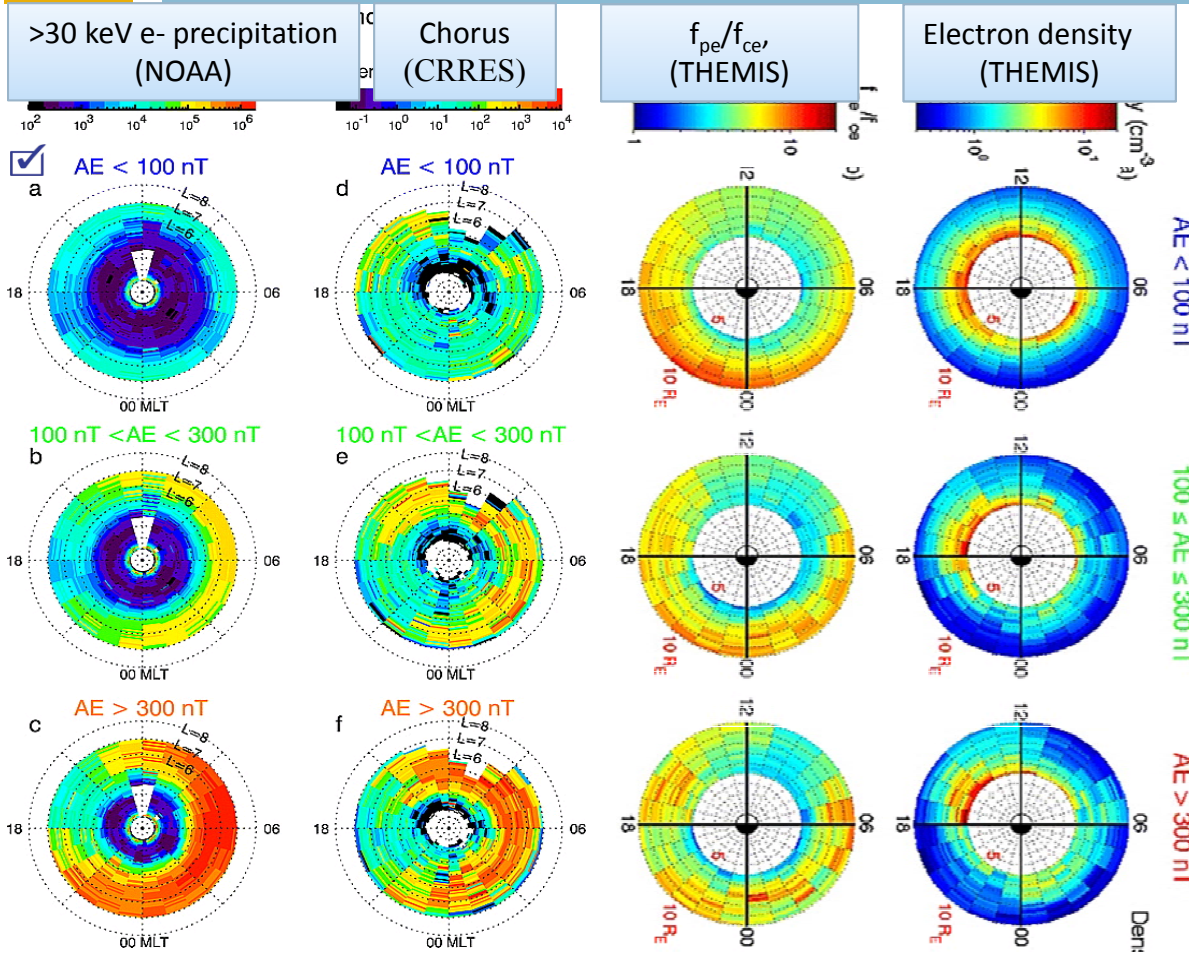


Kasahara et al. (GRL, 2009)

- ~30 keV electrons are injected into the magnetosphere throughout the storm “recovery” phase.
- There is a clear correlation among continuous injection of hot electrons, generation of chorus, geomagnetic AE activity and intensity of relativistic electrons.
- Similar results is obtained by Li et al. (JGR, 2009) who used data from THEMIS satellite.

Hot electrons, cold electrons and chorus

53

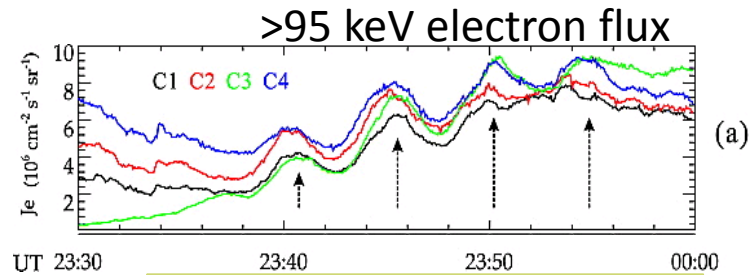


Li et al. (GRL, 2009; JGR, 2010),
Lam et al. (JGR, 2010)

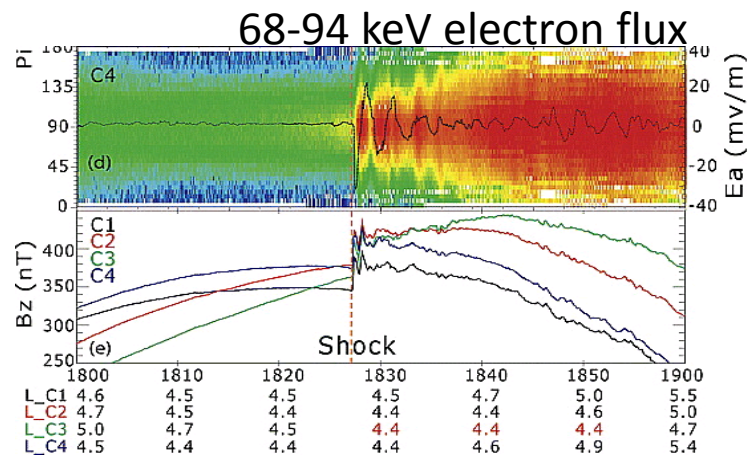
- The global distribution of the precipitating flux of > 30 keV electrons is well-correlated with the global distribution of lower-band chorus waves
- Intensity of chorus waves increases in the region where $f_{pe}/f_{ce} < 5$

Drift resonance with ULF waves

54



Yang et al. (JGR, 2010)

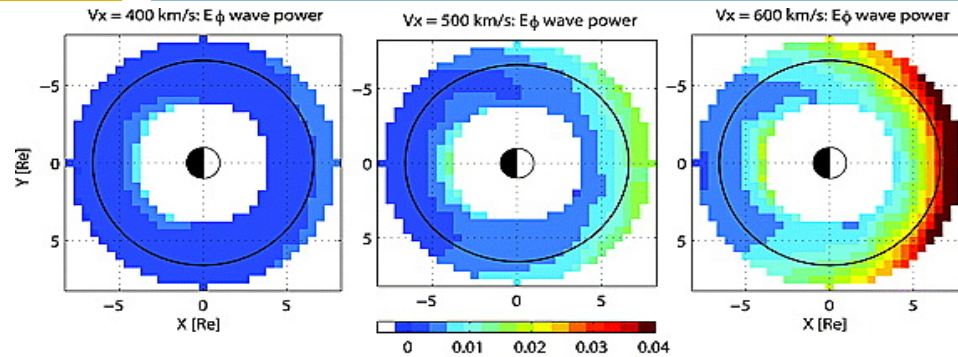


Marshall et al. (JGR, 2010)

- ✓ ■ Drift resonant acceleration by ULF waves is observed.
- Energetic electron fluxes are increased by ULF waves.
- ULF waves also increase outward diffusion (Loto'aniu et al., JGR, 2010).
- The solar wind velocity (not solar wind dynamic pressure) has the strongest correlation with the daily averaged Pc4 and 5 wave magnitude in 4 ~ 9 RE. (Liu et al., JGR, 2010)

MHD-generated ULF waves

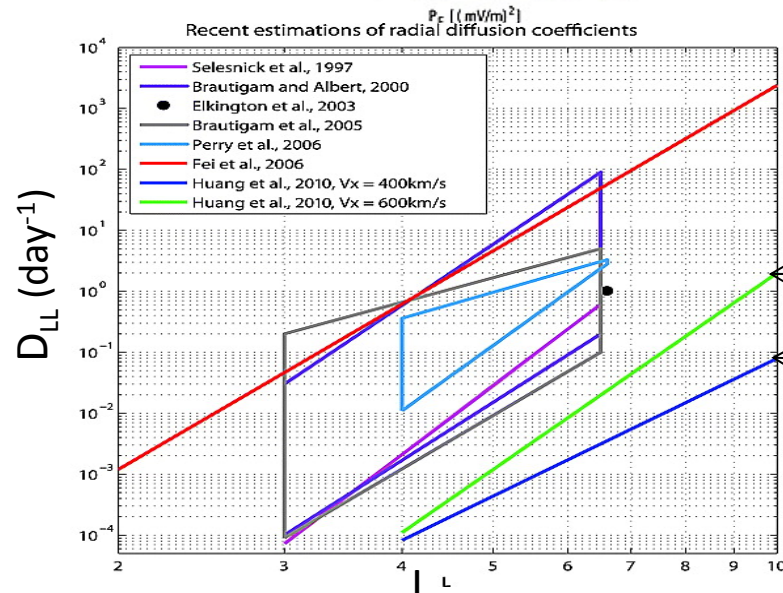
55



Huang et al. (2010a, 2010b)



- ULF waves are generated by MHD simulation (Huang et al., JGR, 2010a, 2010b)



D_{LL} by MHD-generated ULF waves ($V_x=600 \text{ km/s}$)

D_{LL} by MHD-generated ULF waves ($V_x=400 \text{ km/s}$)

Diffusive transport in L, pitch angle and energy

56

- Albert (JASTP, 2009; JGR, 2010)
 - Quasi-linear formulation with a mixed or cross diffusion coefficient
 - Full broadband quasi-linear diffusion coefficients for chorus waves
- Chu et al. (JGR, 2010)
- Ni et al. (JGR, 2009a, 2009b)
 - Data assimilation
- Shprits et al. (JGR, 2009)
 - MLT-dependent Pitch angle diffusion coefficients by chorus and EMIC waves
- Su et al. (JGR, 2009a, 2009b, 2010a, 2010b, 2010c, 2010d, 2011; GRL, 2011; JASTP, 2011),
Xiao et al (JGR, 2009a, 2009b, 2010a, 2010b)
 - STEERB and Hybrid finite difference (HFD) codes
 - Evolution of pitch angle distribution, inclusion of cross pitch angle-energy diffusion, pitch angle scattering by chorus waves, plasmaspheric hiss, and EMIC waves.
- Subbotin et al. (JGR, 2010)
 - Cross diffusion
- Tao et al. (JGR, 2009, 2011; GRL, 2011)
 - “Layer method” is proposed to solve cross diffusion term.
- Tu et al. (JGR, 2009, 2010)

Structure

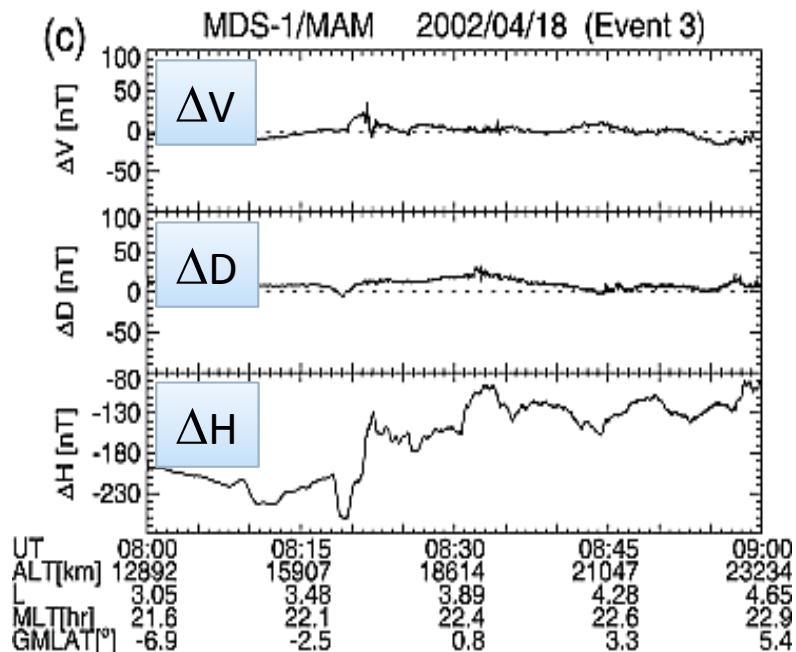
57

- Plasmasphere
- Ring current
- Radiation belt
- **Magnetic and electric fields**
- Challenging issues

Dipolarization in inner magnetosphere

58

Nose et al. (JGR, 2010)

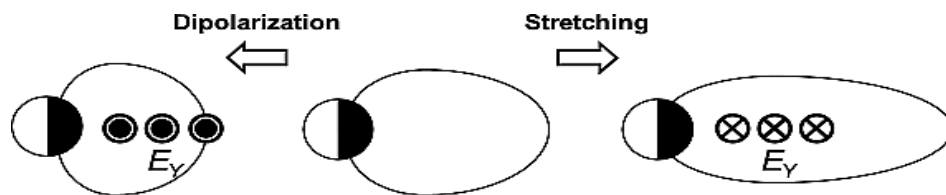
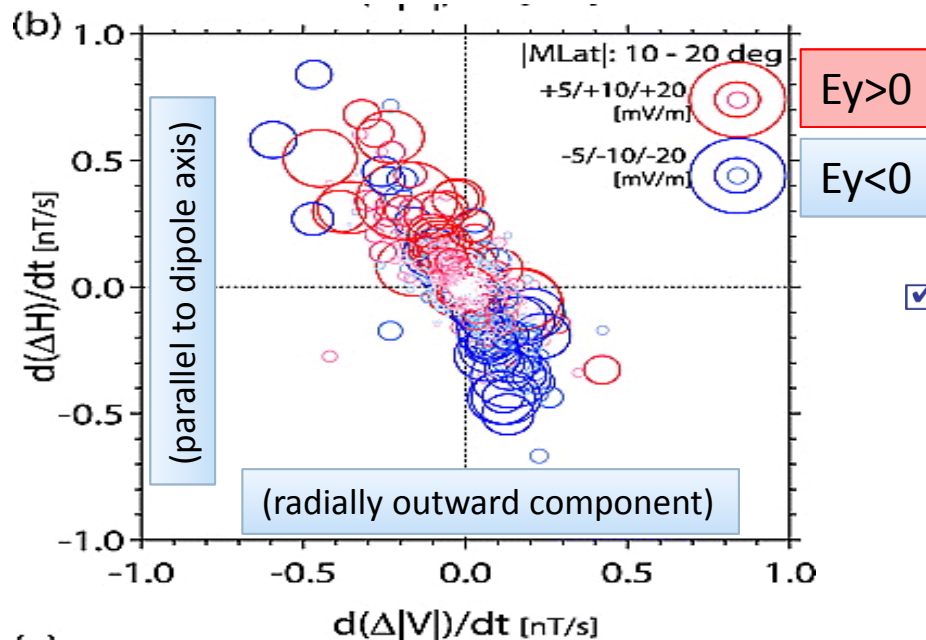


- Data from MDS-1 (GTO satellite) shows
 - dipolarization can be detected at $L=3.5-6.5$
 - dipolarization was accompanied by magnetic field fluctuations having a characteristic timescale of 3-5 s, which is comparable to the local gyroperiod of O^+ ions
- Data from Cluster shows
 - The sign of duskward component of electric field E_y is well organized by the change of magnetic field.
 - When the local magnetic becomes more dipolar, E_y tends to be positive (duskward), whereas it tends to be negative (dawnward) when the configuration becomes more stretched.
 - The electric fields are induction field.

Dipolarization in inner magnetosphere

59

Ohtani et al. (JGR, 2010)



- Data from MDS-1 (GTO satellite) shows
 - dipolarization can be detected at $L = 3.5-6.5$
 - dipolarization was accompanied by magnetic field fluctuations having a characteristic timescale of 3-5 s, which is comparable to the local gyroperiod of O^+ ions



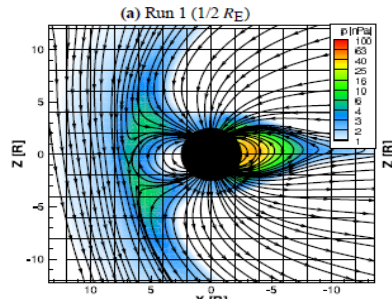
■ Data from Cluster shows

- The sign of duskward component of electric field E_y is well organized by the change of magnetic field.
- When the local magnetic becomes more dipolar, E_y tends to be positive (duskward), whereas it tends to be negative (dawnward) when the configuration becomes more stretched.
- The electric fields are induction field.

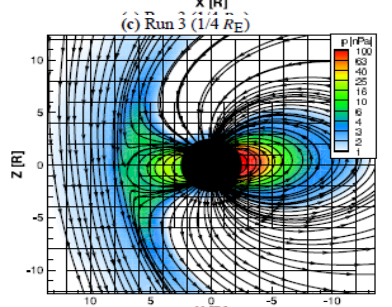
Inner/outer magnetosphere coupling

60

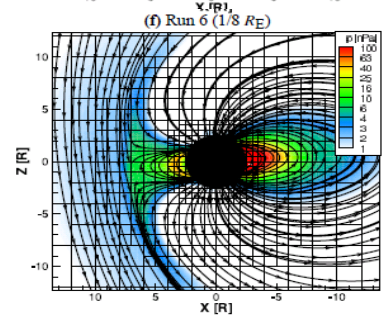
Ridley et al. (AG, 2010)



1/2 Re grid



1/4 Re grid



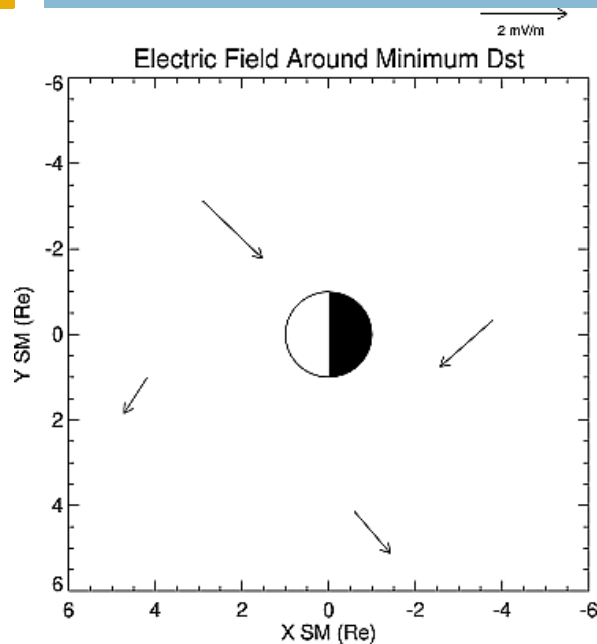
1/8 Re grid

- Even with a very good solver and the highest affordable grid resolution, the inner magnetosphere is not grid converged.
- “many numerical effects work nonlinearly to complicate the interpretation of the physics within the magnetosphere”
- “simulation results should be scrutinized very carefully before a physical interpretation of the results is made”

Lowest resolution gives stretched B-field on the nightside, but underestimates the intensity of the ring current.

Storm-time electric field

61



Matsui et al. (JGR, 2010)

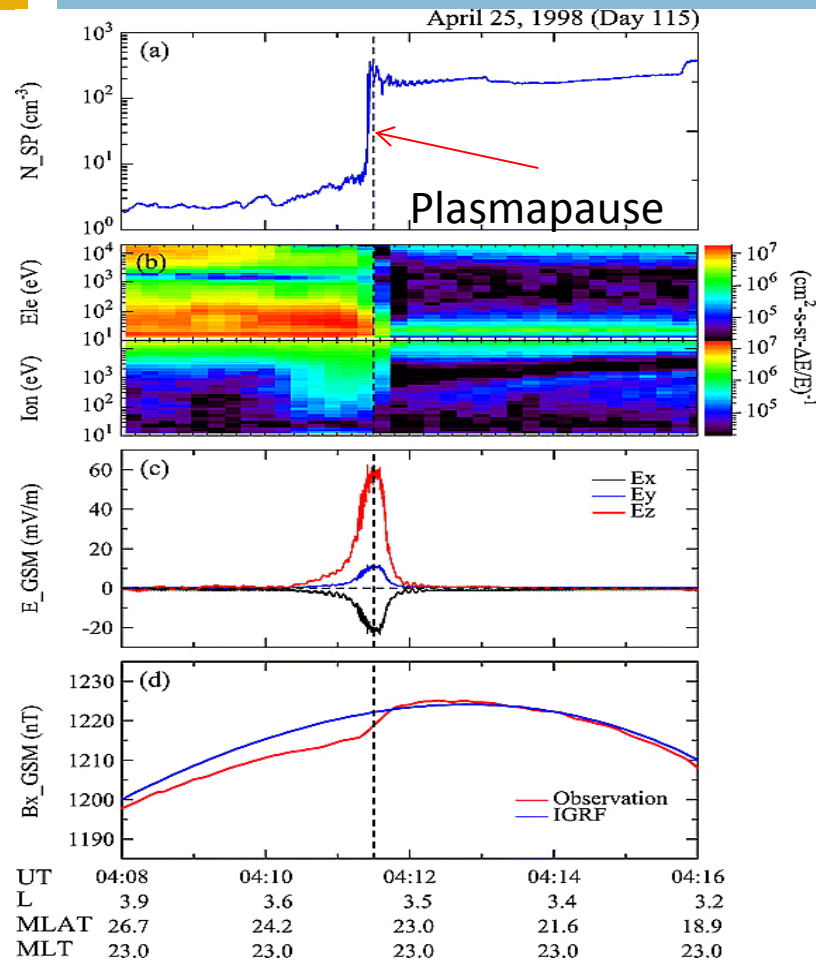
- E-field in the inner magnetosphere is indeed increased during storms (Matsui et al, JGR, 2010)

- Electric field vector observed by Cluster around minimum Dst.
- AC electric fields are generally larger than DC electric fields

Large-amplitude outward electric field

62

Kim et al. (JGR, 2010)



- Large-amplitude electric field, with amplitude 60 mV/m and directing outward, was observed at L=3.5 on the plasmapause.
- The E-field is collocated with eastward current on the plasmapause.
 - Suggesting “plasma pause current?”